Carnegie Mellon University

CARNEGIE INSTITUTE OF TECHNOLOGY

THESIS

SUBMITTED IN PARTIAL FULFILLMENT OF THE REQUIREMENTS

FOR THE DEGREE OF Doctor of Philosophy

TITLE Homogeneous Dislocation Nucleation

PRESENTED BY Akanksha Garg

ACCEPTED BY THE DEPARTMENTS OF

Civil and Environmental Engineering

Craig Maloney	September 10, 2014
CO-ADVISOR, MAJOR PROFESSOR	DATE
jAmit Acharya	September 23, 2014
CO-ADVISOR, MAJOR PROFESSOR	DATE
David A. Dzombak	September 23, 2014
DEPARTMENT HEAD	DATE

APPROVED BY THE COLLEGE COUNCIL

Vijayakumar Bhagavatula	September 25, 2014
DEAN	DATE

Homogeneous Dislocation Nucleation

Submitted in partial fulfillment of the requirements for

the degree of

Doctor of Philosophy

in

Civil & Environmental Engineering Department

Akanksha Garg

B. Tech., Mechanical Engineering, Indian Institute of Technology, Kanpur

M.S., Civil & Environmental Engineering, Carnegie Mellon University

Carnegie Mellon University

Pittsburgh, PA

September 24, 2014

Acknowledgement

Firstly, I wish to thank my advisors Prof. Craig Maloney and Prof. Amit Acharya for their guidance throughout my Ph.D. in research and beyond. Their support encouraged me to push my limits further. I joined CMU as a hardened engineer; Prof. Maloney motivated me to appreciate the science within the engineering. Prof. Acharya helped during the most difficult of times through his feedback, especially while writing this thesis.

I would also like to thank my committee members Prof. Yoosuf Picard and Prof. Elizabeth Holm for motivating me to think forward about relevant experiments and applications of this work. I am grateful to Prof. Jacobo Bielak, Prof. Jack Beuth and Prof. Alan McGaughey for teaching me the fundamentals and guiding me through complications in my research. I would also like to thank Maxine Leffard and Julian Krishnamurti for going out of their way to assist me whenever I needed them.

I gratefully acknowledge the funding sources that made my graduate studies possible. I was funded by National Science Foundation under Award Number CMMI-1100245 for three years and was honoured to be CIT Dean's Fellow and Neil & Jo Bushnell Fellow for the remaining period.

The members of my research group: Dr. Asad Hasan, Dr. Kamran Karimi, Arka Prabha Roy and Navid Kazem have contributed immensely to my personal and professional development at CMU. The group has been a source of good advice, fruitful discussions and collaborations. I would also like to thank my friends: Gagan

Srivastava, Snigdha Chaturvedi, Sneha Prabha Narra, Shashank Srivastava for their support and care during the times of peril and helping me cherish my time here. I really enjoyed my involvement in Society of Women Engineers and the Explorers Club at CMU. Through these organizations, I got a chance to interact with several graduate and undergraduate students at CMU.

Finally, none of this would have been possible without the love and patience of my family. The credit for my ardent interest in mathematics definitely goes to my mother, for assisting and motivating me to solve challenging problems since my childhood.

Abstract

We perform atomistic simulations to study the mechanism of homogeneous dislocation nucleation in crystalline films during nanoindentation. Initially the crystal deforms elastically during nanoindentation and eventually, at some point, it becomes unstable and dislocations nucleate in the bulk of crystal. The velocity field or the critical eigenmode, just before nucleation, is found to be localized along a line (or plane in 3D) of atoms with a lateral extent, ξ, at some depth, Y^*, below the surface, underneath the indenter of radius, R.

In the first chapter of this thesis, we study the effect of interaction potentials and crystal geometry. We use realistic interatomic potentials such as embedded atom method (EAM) potentials for Aluminium (Al) in addition to simple pair-wise interactions such as linear springs. We show that for all interatomic potentials, the macro scale properties i.e. the scaled critical load, F_c/R, and scaled critical contact length, C_c/R, decrease to R-independent values in the limit of large R. However, despite the R independence of F_c/R and C_c/R, ξ/R and Y^*/R display non-trivial scaling with R. We show that although both the interaction potential and the orientation of the lattice affect the *prefactors* in the scaling relations (e.g. the crystal with Hookean springs is much harder than either EAM Aluminum or Lennard-Jones), all the *scaling laws* are robust. We also show that the local strain based Λ criterion of vanVliet et. al. holds equally well for all potentials and orientations. Furthermore, it predicts the polarization of the critical eigenmode with excellent accuracy.

In the second chapter, we present meso-scale analysis, a computationally inexpensive technique to analyze incipient dislocation nucleation. The lowest

energy eigenmode for meso-regions of varying radius, r_{meso}, centered on the localized region of the critical mode is computed. The energy of the lowest eigenmode, λ_{meso}, decays very rapidly with r_{meso} and $\lambda_{meso} \approx 0$ for $r_{meso} \gtrsim \xi$. The analysis of a meso-scale region in the material can reveal the presence of incipient instability even for $r_{meso} \lesssim \xi$ but gives reasonable estimate for the energy and spatial extent of the critical mode only for $r_{meso} \gtrsim \xi$. When the meso-region is not centered on the localized region, called embryo, we show that the meso-region should contain a critical part of the embryo (and not only the center of embryo) to signal instability. This scenario indicates that homogeneous dislocation nucleation is a quasi-local phenomenon. We also observe that meso-scale eigenmode reveals instability much sooner than the full system eigenmode, thus making the simulations much less computationally expensive.

In the third chapter, the kinematic structure of the theory of Field Dislocation Mechanics (FDM) is shown to allow the identification of a local feature of the atomistic velocity field in these simulations as indicative of dislocation nucleation. It predicts the precise location of the incipient spatially distributed dislocation field, as shown for the cases of the Embedded Atom Method potential for Al and the Lennard-Jones pair potential. We demonstrate the accuracy of this analysis for two crystallographic orientations in 2D and one in 3D. Apart from the accuracy in predicting the location of dislocation nucleation, the FDM based analysis also demonstrates superior performance than existing nucleation criteria in not persisting in time beyond the nucleation event, as well as differentiating between phase boundary/shear band and dislocation nucleation. Our analysis is meant to facilitate the modeling of dislocation nu-

cleation in coarser-than-atomistic scale models of the mechanics of materials.

Contents

List of Figures

Chapter 1

Introduction

1.1 Motivation

The mechanisms for plastic deformation in crystals, caused by dislocation motion, have been studied since the 1930's [6] and are fairly well understood. Crystals, at the microscale typically contain thousands of pre-existing defects. In the bulk of these microscale crystals, new dislocations are predominantly produced by multiplication of pre-existing dislocations (called Frank-Read sources) [7]. With the advancement in nanotechnology, namely, the tools such as nano-indentation and microscopy techniques such as SEM and TEM, pristine nano-scale sections of materials are accessible that do not contain any defects. Under appropriate loading conditions, these pristine sections can nucleate dislocations. This process of nucleation of dislocations in the bulk, in the absence of other defects is known as *Homogeneous Dislocation*

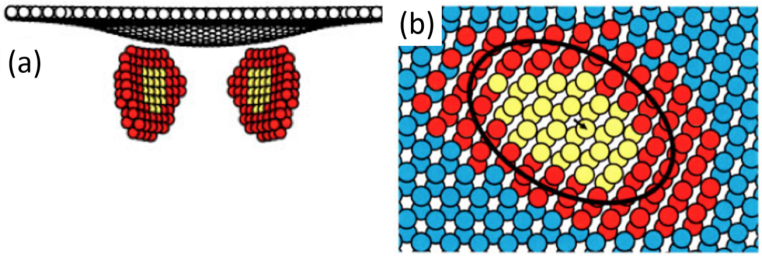

Figure 1.1: These images have been obtained from the work of Kelchner et. al. [1]. The colors in these pictures show centrosymmetry parameter. The red atoms form part of partial dislocations and yellow atoms correspond to stacking faults. (a) Incipient dislocation loops observed during dislocation nucleation at the first plastic yield point on $Au(111)$ (b) (111) planes are slipping against each other for nucleating a dislocation loop.

Nucleation. In past two decades, homogeneous dislocation nucleation (HDN) has been observed by several authors ([1], [8], [9], [10]) through atomistic simulations. Kelchner et. al. [1] observed the structure of incipient dislocation during indentation on $Au(111)$ in their MD simulations, as shown in fig. 1.1. Gouldstone et. al. [2] experimentally demonstrated HDN through a bubble-raft experiment, using a two dimensional crystal made of soap bubbles, as shown in fig. 1.2. Later, Rodriguez de la Fuente et al. [3] showed HDN during nano-indentation of gold films. *Hillocks* stemming from the indentation on Au(001) due to the nucleation of dislocation loops are shown in fig. 1.3.

Under given loading conditions, the motion of dislocations and their growth in the presence of Frank-Read sources is well understood and is considered predictable [7]. However, the material conditions resulting in HDN are not well understood. The

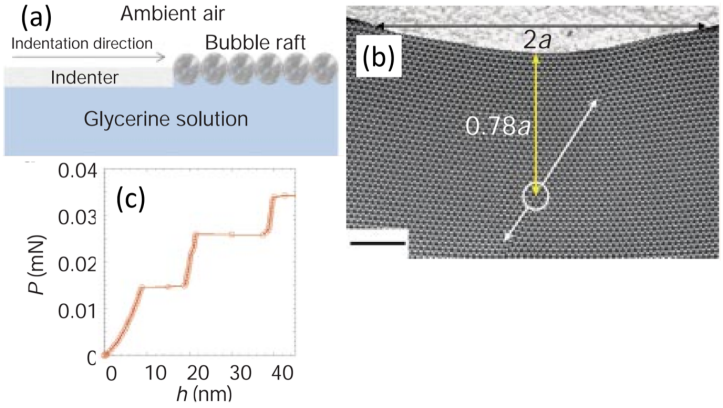

Figure 1.2: These figures have been obtained from the work of Gouldstone et. al. [2] (a) Schematic of indentation on Bubble raft set-up is shown, (b) Initially defect free rafts nucleating dipole of dislocation during indentation (c) Load on the indenter, P, vs. indenter depth, h, during indentation. The discontinuities in the load vs. depth curves correspond to the nucleation events.

question of when and where the dislocations are going to nucleate is relevant for predicting the behavior of various nanoscale materials such as nanowires, nanopillars and nanospheres. Gerberich et. al. [11] studied the dislocation morphology and nucleation in the bulk of Silicon nanospheres. Jennings et. al. [12] have analyzed the size effects of pillar diameter on the strength of nanowires. Jennings et. al. [12] performed simulations of nanowires during homogeneous compression, at a finite temperature and finite strain rate. In their work, dislocation nucleation in the bulk of nanowires is driven by thermal gradients. During compression of nanospheres at finite temperature [11], along with the thermal fluctuations, there is an inhomogeneous strain field in the crystal. In this dissertation, we perform nano-indentation simulations of defect-free crystal films at absolute zero (0 K). Inhomogeneous loading conditions due to the indenter motion result in the nucleation of a dislocation dipole

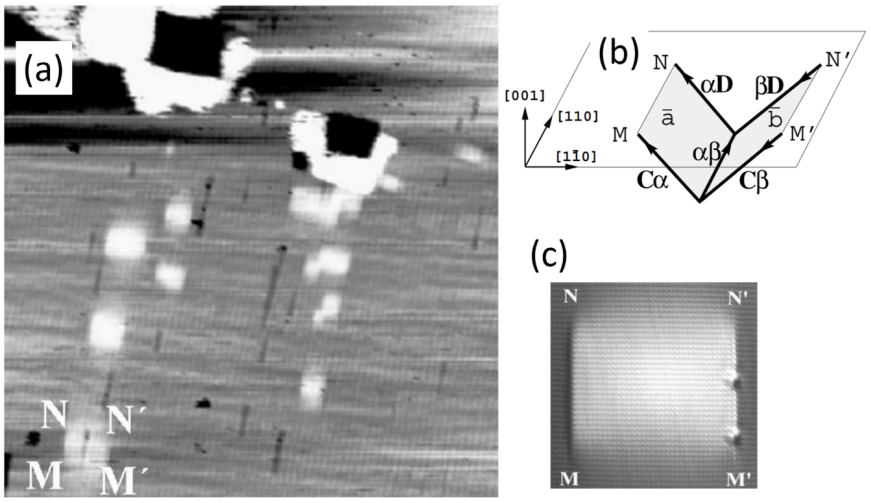

Figure 1.3: These images of nanoindentation on $Au(001)$ have been obtained from the publication by Rodriguez de la Fuente et al[3]. (a) STM image of two nanoindentations on $Au(001)$ surfaces. Bump like features, called Hillocks, arising from indentation. (b) STM image of one of the Hillock, seen near the indentation point. (c) Dislocation nucleation configuraion proposed for creating the Hillock shown in (b).

(in 2D) or a dislocation loop (in 3D).

1.2 Problem statement

Dislocation nucleation has been studied for the past two decades, but surprisingly, still not that well understood. To overcome this limited understanding, multiple research questions have been addressed in this dissertation:

1) Is it the material (inter-atomic potential), or the geometrical conditions (e.g. indenter radius, crystal structure), that are more important for these instabilities? In continuum mechanics, one can distinguish between the material and the geometrical part of the stiffness matrix when the governing equations are written in a particular way. However, in atomistic systems there is no methodology to achieve this. Can dislocations nucleate in a Hookean crystal, where the particles are connected by harmonic springs?

2) How does the hardness of a defect-free crystal film depend on the indenter radius? How does the incipient dislocation loop location and structure depend on the indenter radius? A related question is, what is the effect of interatomic potentials and crystal orientations on these scaling laws?

3) How good is Hertzian contact mechanics for predicting nano-indentation atomistic simulations? Can Hertzian contact mechanics predict the strains upto instability? If not, upto what indenter depth can Hertzian contact mechanics be used?

4) Is the instability local, i.e. breaking of the bond between any two atoms, or global, as in the case of buckling of the whole chain of atoms during compression? In other

words, can we observe the material in a small region and predict instability? If yes, what should be the size of meso-region to be analyzed? How good is this meso-scale analysis in terms of computational efficiency?

5) Should one use a criterion based on the local resolved shear stress as used for the motion of pre-existing dislocations? Or is a criterion based on the gradient of the stress field more appropriate for defect creation? More generally, can the criterion be phrased in a local way at all, or must one look at the global loading geometry as in the case of buckling of an Euler beam?

6) Can we extract some kind of material parameter, or rule, that encodes the threshold for elastic instability? How can this rule be used in coarse-grained schemes such as Field Dislocation Mechanics?

1.3 Significance of this research

Atomistic scale models provide insight to higher scale models, such as: models based on Discrete Dislocation Dynamics and Cauchy-Born rule [13]. As discussed in the later chapters of this work, Field Dislocation Mechanics embodies HDN within the theory to develop a criteria for predicting the location and instant of HDN. A criteria based on meso-scale analysis in chapter 3 could serve as an outline for including the atomistic details at the dislocation embryo in coarser-than-atomistic models. The non-linear scaling laws for the incipient dislocation loop in chapter 2 show the importance of lattice constant in higher scale models. A theory that involves the indenter radius (R) as the only length related input parameter would be capable of

predicting these non-linear scaling laws.

The results obtained from the atomistic simulations in this work can be used to guide nanoindentation experiments. At such small scales, much remains unclear about the kind of measurements required for identifying HDN. For instance: resolved shear stress, used predominantly for dislocation motion, cannot be used for predicting HDN. This work contains a review of several quantities such as: stress gradients, Hill's continuum planewave stability criterion, velocity gradients to equip experiments with different methodologies to study HDN. It is often challenging to determine whether the observed nano-scale mechanical response in experiments is the result of *homogeneous* or *heterogeneous* dislocation nucleation [**?**]. The non-linear scaling laws for embryo location given in chapter 2 can be potentially verified in experiments. These scaling laws can be used to identify whether the nucleation of new dislocations is in truly pristine materials or involves interaction with pre-existing ones.

1.4 Dissertation structure

This dissertation is organized as follows. Each chapter forms a self contained paper, having an "introduction - modeling - methodology - results - conclusion" format. Chapter 2 examines the research questions 1, 2 and 3. The nucleation of dislocations in two dimensional crystals has been observed for different interatomic potentials, including the Hookean potential. In chapter 2, it is shown that the scaling laws for

incipient dislocation loop remain the same, irrespective of the interatomic potentials and crystal orientations.

In chapter 3, research questions 4 and 5 are addressed. Dislocation nucleation is shown to be a meso-scale process. A computationally efficient, meso-scale analysis technique is developed to analyze the properties of the incipient dislocation nucleation. The applicability of this technique is demonstrated for three dimensional nano-indentation simulations of an FCC lattice for one crystal orientation.

Chapter 4 contains the linear stability analysis of the evolution equation of the dislocation density tensor in Field Dislocation Mechanics (research question 6). This analysis predicts the location, and the instant of dislocation nucleation for all considered interatomic potentials and crystal orientations. This analysis can be used to model HDN in coarser-than-atomistic models.

Chapter 2

Universal scaling laws for homogeneous dislocation nucleation during nano-indentation

2.1 Introduction

Nanoindentation has become an increasingly important tool in recent years to characterize the mechanical response of materials. With the advancement in microscopy techniques (eg. TEM), it is possible to make concurrent measurements of load and structure during the indentation process. In this work, we focus on the ideal case where the material subject to indentation contains no pre-existing defects; voids, dislocations, or grain boundaries. It is possible to realize this situation experimentally in films that are on the order of thousands of atoms thick. Rodriguez de la Fuente et al. [3] performed these type of indentation experiments on Au. They showed nucleation of dislocations *inside* the Au sample and compared their sample after the plastic yielding events with the atomistic simulations. Gouldstone et. al. [2] also showed homogeneous dislocation nucleation events in 2D bubble raft experiments. Kelchner et al. [1] were the first to show the dislocation embryos during the indentation of Au in atomistic simulations.

In these experiments and simulations, the question of where in the sample and under what conditions these instabilities nucleate is still surprisingly contentious. Moreover, it is not understood at all if the material, as in the motion of a pre-existing dislocation on approach to the Peierls threshold, or the system geometry, as in the Euler bucking of a column, determines the threshold for nucleation of these instabilities.

In this work, we focus on the initial *elastic bifurcation* event. The bifurcation event is accompanied by nucleation of a dislocation dipole in 2D or a dislocation loop in 3D. The nucleation process is governed by the vanishing of energy associated with

a single eigenmode, called the critical mode. The incipient dislocation structure observed in the critical mode is called as the embryo.

We show that the geometry and loading conditions play a much more important role than the interatomic interactions in the crystal. We study the scaling laws for critical quantities such as: load, contact length, location and size of the incipient dislocation loop at nucleation with indenter radius, R. We show that, these scaling laws remain consistent for all the interatomic potentials such as embedded atom method (EAM) potentials for Al in addition to simple pair-wise interactions such as Lennard-Jones. Only the prefactors are governed by the interatomic interactions.

The critical quantities considered in this work include hardness, F_c/R, critical contact length, C_c/R, depth of the embryo from surface, Y^* and size of the embryo, ξ. For large values of R, we show that the critical indenter load, F_c, and the contact length, C_c, scale linearly with R, but the increase of Y^* and ξ is non-trivial. Y^* can be potentially determined in experiments by measuring the location of the first surface step formed from the indentation axis. These scaling laws for Y^* and ξ need to be verified in macro-scale models inherently using interatomic potentials (as used in, e.g., reference [8]).

Many authors have also attempted to formulate a nucleation criterion to predict elastic instability. Early simulations showed that simple criterion based on the atomic level resolved shear stress, or Schmid factor, to be incorrect [1]. Later, Li et. al. [8] introduced the Λ criterion, which was based on Hill's analysis [14] of the stability of plane waves in a homogeneously deformed solid. For any homogeneously deformed

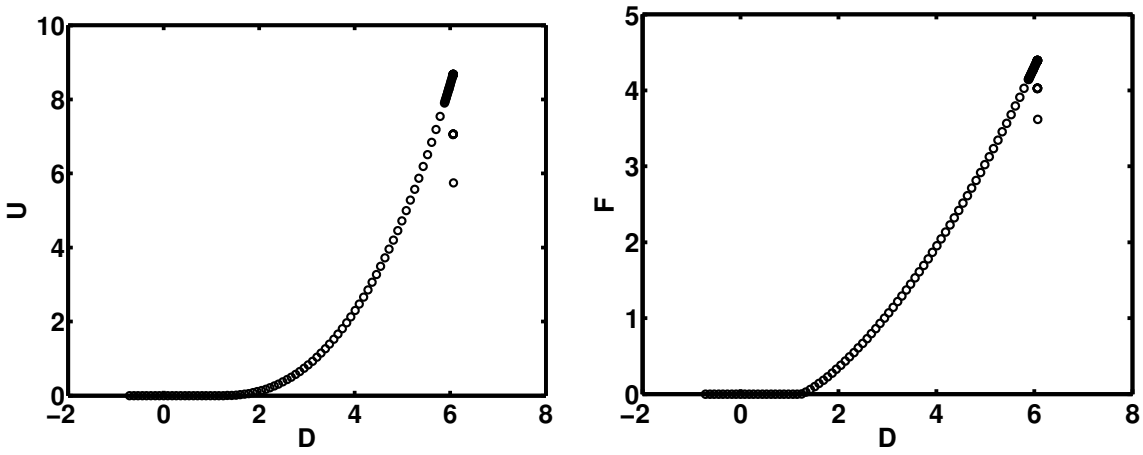

(a) (b)

Figure 2.1: (a) Elastic energy, U, stored in the crystal as a function of indenter depth, D, LJ crystal, $L = 40$, $R = 40$. (b) Corresponding load, F, on the indenter in the vertical direction as function of indenter depth, D.

crystal, Λ is related to the vibrational frequencies of phonons in the crystal and negative values imply instability. In the seminal papers by Zhu, Li and coauthors [8] [15] [13], it was shown that the Λ criterion works well for indentation along the $< 111 >$ axis in FCC copper crystal for EAM, Mishin and Ackland potentials.

However, recently Miller and Rodney [10] pointed out some inconsistencies with the Λ criterion. They showed that Λ becomes negative before the onset of instability for EAM aluminum crystals. This presents a major conceptual difficulty in using Λ criterion as a rigorous indicator of mechanical instability. They also showed that it incorrectly predicts the location of nucleation for EAM aluminum with an unstable surface orientation.

Here we present results on 2D fully atomistic simulations for EAM aluminum lattice

using the same parameters that were used by MR, our results differ qualitatively. We observe that the minimum value of Λ indeed predicts the location of the embryo correctly, even though it becomes negative before dislocation nucleation. On one hand, since Λ becomes negative before nucleation it cannot be used as a nucleation criterion. On the other hand, the fact that Λ predicts the embryo location precisely for all the potentials and orientations makes it very useful. Furthermore, we show here that Λ can also predict slip-plane normal and direction of slip at the embryo with excellent accuracy.

In section 2.2 we describe the modeling details and loading protocol for the various crystal orientations and interatomic potentials. In section 2.3 we present a kinematic description of the mechanism of HDN and our method for defining the embryo size. In section 2.4 we look at the scaling of the critical quantities described above with respect to the indenter radius for all our simulations. We then show in section 2.5 in precisely what sense Λ does work as a predictor for dislocation nucleation, followed by a brief summary and outlook in section 2.6.

2.2 Simulation Formalism

We perform athermal quasi-static nano-indentation simulations for 2D hexagonal crystal films via energy minimization dynamics. The LAMMPS molecular dynamics framework [16] is used to perform non-linear energy minimization with the Polak-Ribiere algorithm, and a custom python code was developed to perform eigen-

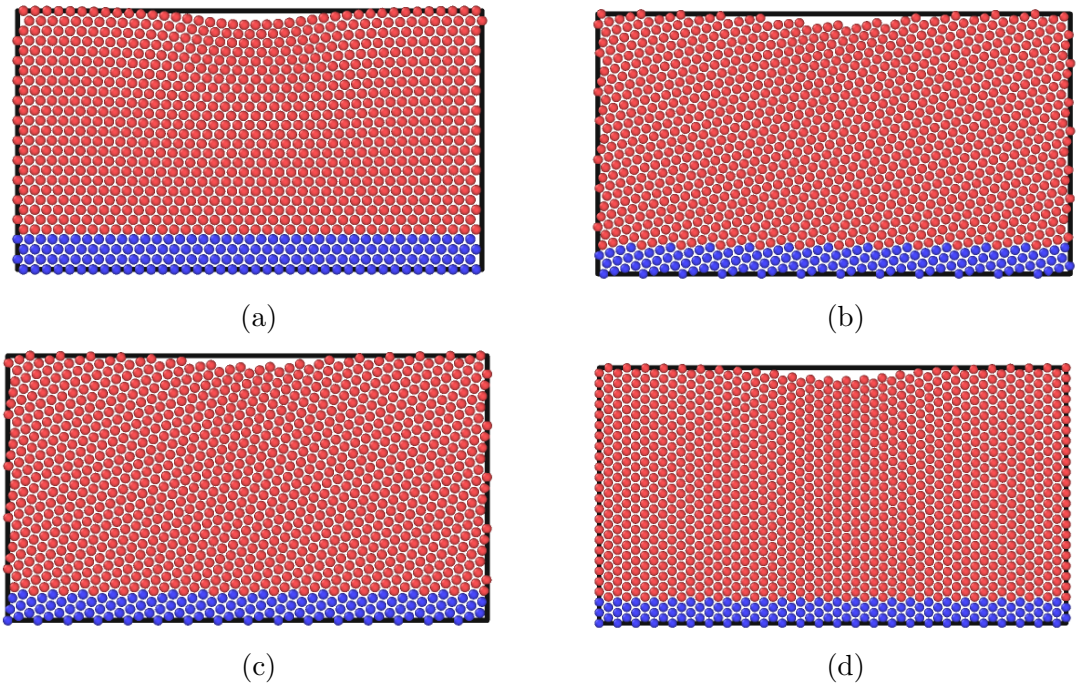

Figure 2.2: Schematic of 4 different orientations of crystal with respect to indenter axis. The red atoms correspond to the crystal and the blue atoms correspond to the rigid base a) O_1 b) O_2 c) O_3 d) O_4

mode analysis using the sparse matrix routines in SciPy [17]. The resulting load-displacement and elastic energy-displacement curves for a typical indentation process are shown in fig. 2.1. The force on the indenter and total potential energy in the crystal increase as the indenter moves into the crystal until the crystal becomes unstable. At the point of instability, the load and potential energy each undergo a discrete, discontinuous drop. The load drop is accompanied by the nucleation of a dislocation dipole as in fig. 2.5a. In this work, we are interested in the structure of the unstable mode precisely at the onset of instability. To reach as close as numerically possible to the nucleation event, we use a dynamic indenter stepping algorithm similar to the algorithm used by MR [10] [8]. When nucleation occurs, we return the indenter to its last stable position before nucleation, reduce the step size by a factor of 10 and restart our simulation.

We configure 2D hexagonal crystals as shown in fig. 2.2 and 2.3 with periodic boundaries on the sides, rigid base at the bottom, and a circular indenter on top of the crystal. The geometrical parameters are shown in the setup diagram in fig.2.3. We chose wide enough L_x that it did not change results significantly. In the rest of the document all the length parameters such as: L_x, L, R and C are measured in units of lattice constant, a. Energy is measured in units of Ea^2 where E is the 2D Young's Modulus for each interatomic potential crystal (see Appendix C).

We use a stiff, featureless, harmonic, repulsive, cylindrical indenter for all our simulations as in ([5], [10]). The interaction potential used to model the interaction

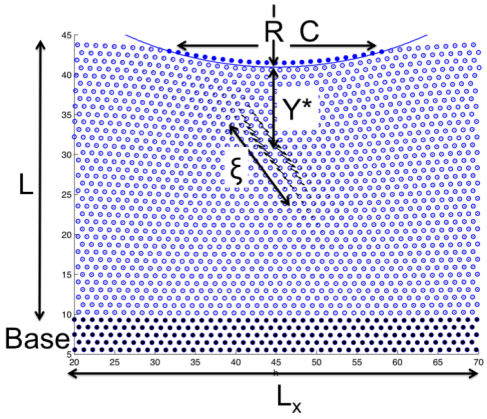

Figure 2.3: Schematic of the setup. All the relevant geometrical parameters are shown: crystalline film width, L_x; film thickness, L; indenter radius, R; contact length, C; the crystal orientation with respect to indenter motion axis, O.

between the indenter and the atoms is of the form:

$$\begin{aligned} \phi(r) = A(R-r)^2 \quad & if\ r <= R, \\ 0 \qquad & if\ r > R \end{aligned} \tag{2.1}$$

Here, R is the indenter radius and r is the distance of the particle from indenter center. Therefore, $R - r$ is the distance of closest approach of the particle to the indenter surface. We set A to be large enough that it does not affect any results but small enough that it does not cause numerical difficulties during the energy minimization procedure.

We study 4 different crystallographic orientations which we label: O_1, O_2, O_3, O_4 as shown in fig. 2.2. O_1 has the nearest neighbor axis aligned normal to the indenter motion axis. In O_2 and O_3 the nearest neighbor axes are roughly aligned at 14°and 19° respectively from the indentation direction. In O_4 the nearest neighbor axis is

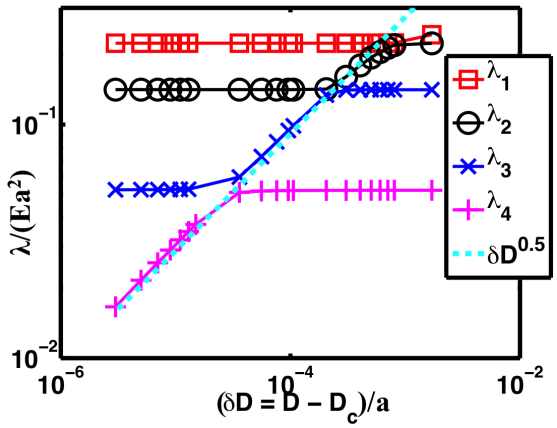

Figure 2.4: Lowest 4 energy eigenvalues, λ, for $L = 40, R = 40$, O_1, LJ crystal, as function of $\delta D = D - D_c$. The cyan line is a fit to $\lambda \approx (\delta D)$.

parallel to the indentation direction. Note that the surfaces of O_2, O_3 and O_4 are much rougher than the surface of O_1.

To study the effect of the form of the interatomic interactions on the nucleation process we use 4 different potentials: Lennard-Jones (LJ), Morse, Harmonic (or Hookean), and an EAM potential. In the LJ and Harmonic potentials, there are no free parameter. For Morse, the exponential coefficient, α, is 10 in our simulations. We use the Ercolessi-Adams EAM potential for Al. [18].

2.3 Kinematic Description of Dislocation Nucleation

The total potential energy, $U(x_{i\alpha}, D)$, is a function of atomic positions, $x_{i\alpha}$, and indenter depth, D. The first derivative of energy with respect to the particle position

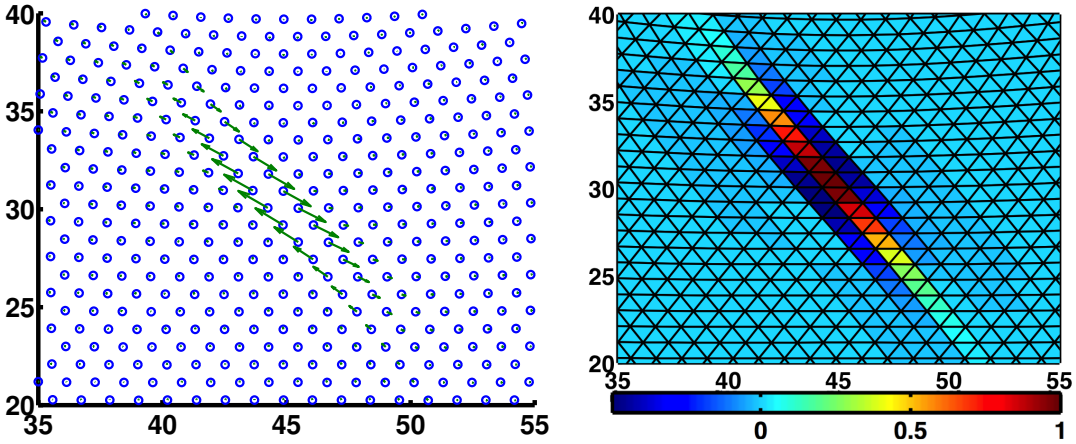

(a) (b)

Figure 2.5: (a) Lowest eigenmode at $\delta D = D - D_c \approx 10^{-6}$ for $L = 40, R = 40$, O_1, LJ crystal.
(b) Corresponding transverse mode gradient, Ω/Ω_{max}.

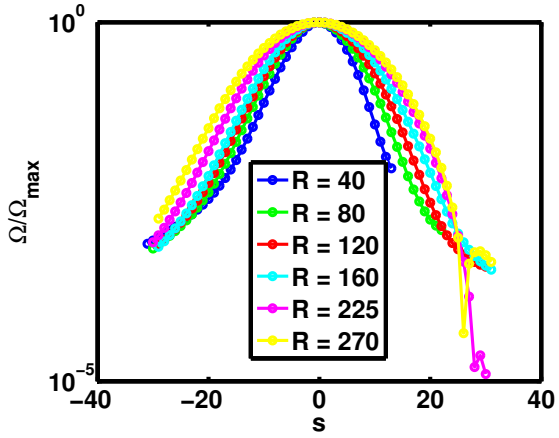

Figure 2.6: Transverse mode gradient, Ω/Ω_{max}, vs. distance, s, along embryo for $L = 80$, O1, LJ crystal.

gives the force, $F_{i\alpha}$, on each particle as:

$$F_{i\alpha} = -\frac{\partial U}{\partial x_{i\alpha}} \tag{2.2}$$

Latin characters are used to index particle number, and Greek characters to index Cartesian components. Then, we use the Lanczos algorithm, as implemented in the SciPy toolkit [17], to compute the lowest 4 eigenvalues of the Hessian matrix for the relaxed configuration at each indenter step.

$$H_{i\alpha j\beta} = \frac{\partial^2 U}{\partial x_{i\alpha} \partial x_{j\beta}} \tag{2.3}$$

The forces induced by an infinitesimal external indenter motion, $\Xi_{i\alpha}$, must be balanced by the internal atomic rearrangements as shown in [19]: .

$$\begin{aligned} \Xi_{i\alpha} &= -\frac{\partial F_{i\alpha}}{\partial D} \\ H_{i\alpha j\beta}\dot{x}_{j\beta} &= \Xi_{i\alpha} \end{aligned} \tag{2.4}$$

Here, $\dot{x} \doteq \frac{dx}{dD}$. We refer to the derivative of the particle positions with respect to indenter depth as *velocities* since D plays the role of *time* in quasi static indentation. We may solve (2.4) at each indentation step to compute the atomic velocities. The analytical expression of $H_{i\alpha j\beta}$ can be simply derived for pair potentials such as LJ potential and Morse Potential using (2.5) [20]

$$M_{i\alpha j\beta} = (c_{ij} - \frac{t_{ij}}{r_{ij}}) n_{ij\alpha} n_{ij\beta} + \frac{t_{ij}}{r_{ij}} \delta_{\alpha\beta} \tag{2.5}$$

where t and c are the first and second derivatives of the bond energy and $n_{ij\alpha}$ is the unit normal pointing from particle i to particle j. Then, $H_{i\alpha j\beta} = -M_{i\alpha j\beta}$ for off diagonal terms and $H_{i\alpha i\beta} = \sum_j M_{i\alpha j\beta}$ for diagonal terms. However, for multibody potentials like EAM potential the calculation of Hessian matrix is more involved. We outline the analytical form of the Hessian matrix for EAM type many-body potentials in Appendix A.

We compute the lowest 4 eigenvalues of the Hessian matrix for the relaxed configurations at each indenter step. In all cases, we observe that the system is driven to instability along a single eigenmode. This mode shows anti-parallel motion of a small number of atoms on adjacent crystal planes as shown in fig. 2.5. This ultimately results in the emission of a pair of edge dislocations after the system is driven past the point of stability. We denote the critical depth, D_c, as the depth of the indenter at which the dislocation dipole nucleates. Then, $\delta D = D - D_c$ is the distance of the indenter from the critical depth. It was shown earlier by Hasan and Maloney [19] that in this case of dislocation nucleation, the bifurcation mechanism is saddle-node type. In a saddle-node bifurcation, a single eigenmode descends through the spectrum, and its eigenvalue vanishes as the square root of the distance to the bifurcation point. We call the energy-eigenmode corresponding to the eigenvalue vanishing as $\delta D^{0.5}$, the critical mode. In fig. 2.4 the critical eigenvalue corresponds to the cyan line.

To calculate the precise location and size of the embryo we define a scalar quantity Ω. For a given vector field, Ω, is the transverse derivative of the vector field along a particular crystal axis in the deformed configuration. The lattice is first triangulated,

and on each triangle, Ω is computed by linear interpolation of the critical mode. Fig. 2.5b, shows Ω corresponding to the mode shown in fig. 2.5a. As expected, Ω is maximum at the center of the embryo. We define the center of the embryo to be at the centroid of the triangle with maximum Ω. s is defined as the distance of each triangle from the triangle corresponding to the maximum Ω along the crystal axis of interest. Fig. 2.6 shows $\Omega(s)$ for $L = 80$ at various R for LJ in orientation O_1. Note that the width of these Ω profiles increases with indenter radius and have a roughly Gaussian form near the embryo center. To define the embryo size, these $\Omega(s)$ profiles are fit to Gaussian functions of the form:

$$\Omega(s)/\Omega_{max} = e^{-s^2/\xi^2} \tag{2.6}$$

We fit the log $\Omega(s)$ curves out to their half-maximum using the generalized least square method to define, ξ, the embryo size. It is important to note that we look at configurations just *before* nucleation. The strain, although large, is quite uniform in the vicinity of the embryo, and these atomic configurations would have almost perfect centrosymmetry [1] and almost vanishing slip vector [21]. Ω is roughly analogous to a slipping *rate* rather than a slip.

2.4 Scaling Analysis

Here, we study the dependence of $\frac{F_c}{R}$, $\frac{C_c}{R}$, $\frac{\xi}{R}$ and $\frac{Y^*}{R}$ with R. First, we ask how well linear contact mechanics describes F and C vs. D before the bifurcation. The

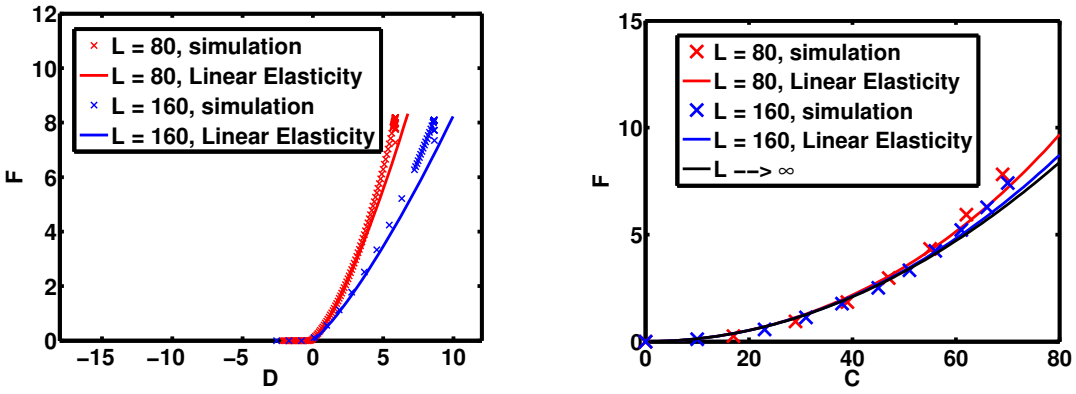

(a) (b)

Figure 2.7: (a) Indenter load, F, as a function of contact length, C (b) Indenter load, F, as a function of indenter depth, D for various L, $R = 160$, O_1, LJ crystal. Solid lines are the predictions of Hertzian contact theory (eq. 2.7 and eq. 2.8)

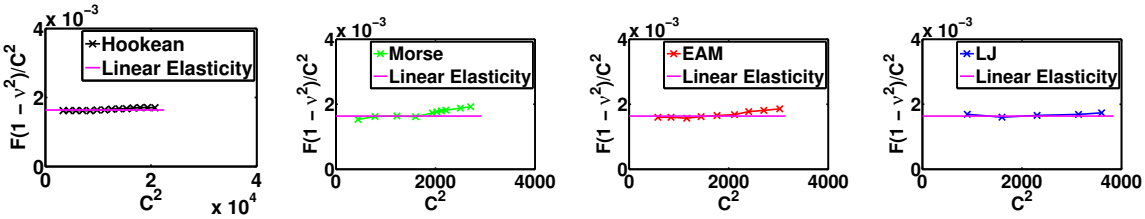

(a) (b) (c) (d)

Figure 2.8: Load as a function of square of contact length, C^2, for different interatomic potentials. The horizontal lines indicate the value of $F(1-\nu^2)/C^2$ given by Hertzian contact theory in the limit of infinite L (eq. 2.7) [4].

analytical expressions for load and indenter depth for a thick linear elastic isotropic infinite layer being indented by a long cylinder were developed by Meijers [4]. Equations 2.7 and 2.8 give load and indenter depth respectively as a function of indenter radius, R, contact length, C, layer thickness, L, and material properties, E (Young's Modulus) & ν (Poisson's Ratio). In these equations α_0, α_1, α_2 are dependent on ν and are given in [4]. For a central force pair potential on a hexagonal lattice, ν is 0.25 and α_0, α_1, α_2 are -2.27, 5.4 and -7.24 respectively. Note that in equation 2.8, D has logarithmic divergence with L.

$$F = \frac{\pi C^2 E}{16R(1-\nu^2)}[1 + 1/8 * \alpha_1(C/2L)^2 + 1/64(\alpha_1^2 + 6\alpha_2)(C/2L)^4] \tag{2.7}$$

$$D = C^2/4R\Bigg(\Big(1/2 + 1/16\alpha_1(C/2L)^2 + 1/128(\alpha_1^2 + 6\alpha_2)(C/2L)^4\Big)ln(8L/C)$$
$$+1/4 + 1/4\alpha_0 + 1/64\alpha_1(3 + 2\alpha_0)(C/2L)^2 + 1/512(2\alpha_0\alpha_1^2 + 12\alpha_0\alpha_2 + 3\alpha_1^2 + 10\alpha_2)(C/2L)^4\Bigg) \tag{2.8}$$

In fig. 2.7a, we study the variation of F vs. D for $R = 160$, LJ-O_1. We see that Hertzian theory gives a good description of load vs. depth with a slight but systematic underestimation of the load just before nucleation. Note that since D has a logarithmic divergence with L in Hertzian theory, it is more convenient to study F vs. C as there is much more rapid convergence to the well defined infinite L limit, and we plot this in fig. 2.7b. In general, we can expect L independence in the F vs. C curves when $L >> C_c/2$. We show below that for all of our samples, C_c $R/2$, so as long as $L >> R/4$, we can expect L independence in the F vs. C curves.

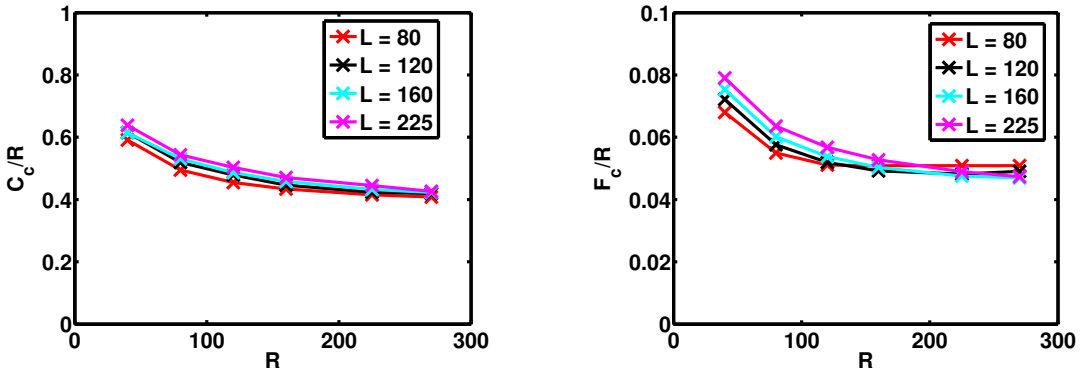

(a) (b)

Figure 2.9: (a) Critical contact length, C_c, as a function of indenter radius, R, for various L, O_1, LJ crystal . (b) Indenter Force, F_c, in the last stable configuration scaled by indenter radius, R, as a function of R for different system sizes, O_1, LJ crystal.

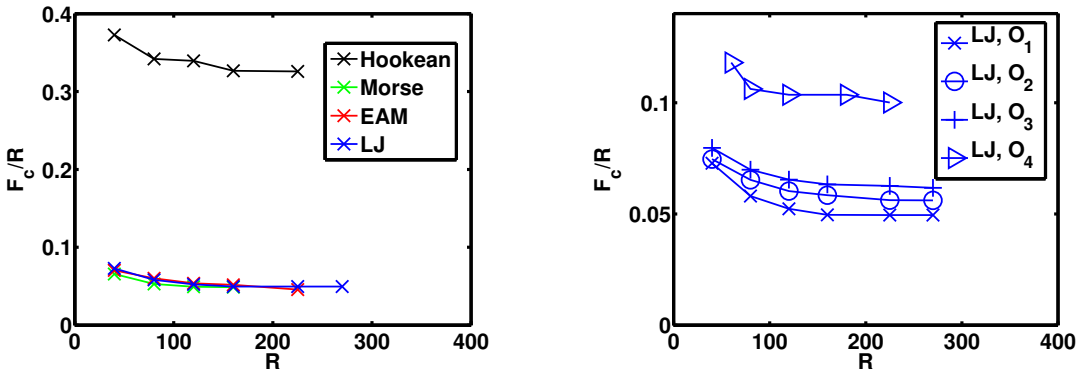

(a) (b)

Figure 2.10: Critical force, F_c, scaled by R as a function of R for $L = 160$ (a) various interatomic potentials (b) various orientations.

For these 2D systems, we define *hardness* as the ratio of critical load, F_c, to the indenter radius, R. In fig. 2.9, we plot the critical load and contact length as a function of indenter radius for various sample sizes. As explained above, within linear contact mechanics, F is determined by C, R and L. So as long as we are in the $L >> R$ limit and linear contact mechanics applies, the critical load, F_c, should be determined by the critical contact length, C_c, and indenter radius, R. When $R > 100$ we observe collapse of hardness, F_c/R, for various L as shown in fig. 2.9b for LJ-O_1. For this range of R as observed in fig. 2.9a, C_c varies linearly with R, and according to equation 2.7 F_c varies as C_c^2/R. Therefore, hardness also remain independent of R as can be seen in fig. 2.9b. For small indenter radii ($R < 100$), the crystal film is relatively harder and indentation size effect (ISE) is observed in both C_c/R and F_c/R curves (fig. 2.9)

We calculate hardness values for different interatomic potentials and non-dimensionalize them by their Young's Modulus, E, calculated for the initial undeformed crystals. The variation of this nondimensional hardness as a function of R for different interatomic potentials and orientations is shown in fig. 2.10. The fact that the nondimensional hardness values for different potentials are not equal even though the nondimensionalized F vs. C curves for all the potentials approximately collapse up to nucleation (fig. 2.10 and 2.8), indicates the importance of non-linear behavior of interatomic potentials for determining the prefactors. It is interesting that the harmonic crystal has the highest non-dimensionalized hardness, and thus provides us limiting value estimates of the hardness. Among different orientations, the most stable surface orientation, O_1, has the lowest hardness value. O_4, for which the indenter

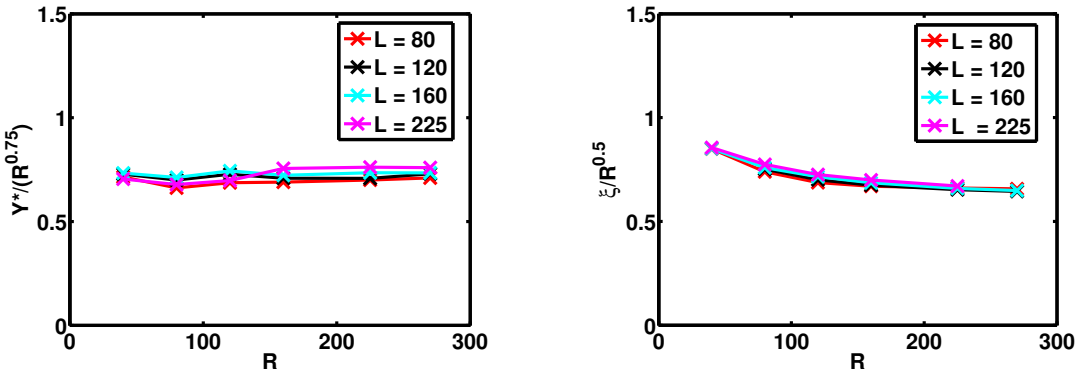

(a) (b)

Figure 2.11: (a) Depth of embryo center, Y^*, scaled by $R^{0.75}$ (b) Embryo size, ξ, scaled by $R^{0.5}$ - as a function of R for different system sizes, O_1, LJ crystal.

axis is parallel to the crystal axis has roughly twice the hardness of O_1.

Previous authors ([10], [22]) have employed quasicontinuum simulations for significantly large system size regime such that their results are independent of L. For EAM potential MR observed F_c/C_c to be between 0.28 ev/A^{o3} - 0.33 ev/A^{o3} for the systems that were two order of magnitude bigger than our systems. For our $L = 120$, $R = 120$ EAM potential crystal F_c/C_c is found to be 0.29 ev/A^{o3} that matches well with MR. Our simulation results clearly show that if L is bigger than 100, the system size effects are no longer important and fully atomistic simulations can yield the required information. For the range of R of interest, we also calculate C_c using linear elasticity for known F_c and R. F_c/C_c using this linear elastic calculation is 0.25 ev/A^{o3} which is roughly 13% lower than the actual value showing that deviation from linear contact mechanics are non-negligible.

We measure depth of the embryo from the bottom most point of the deformed surface,

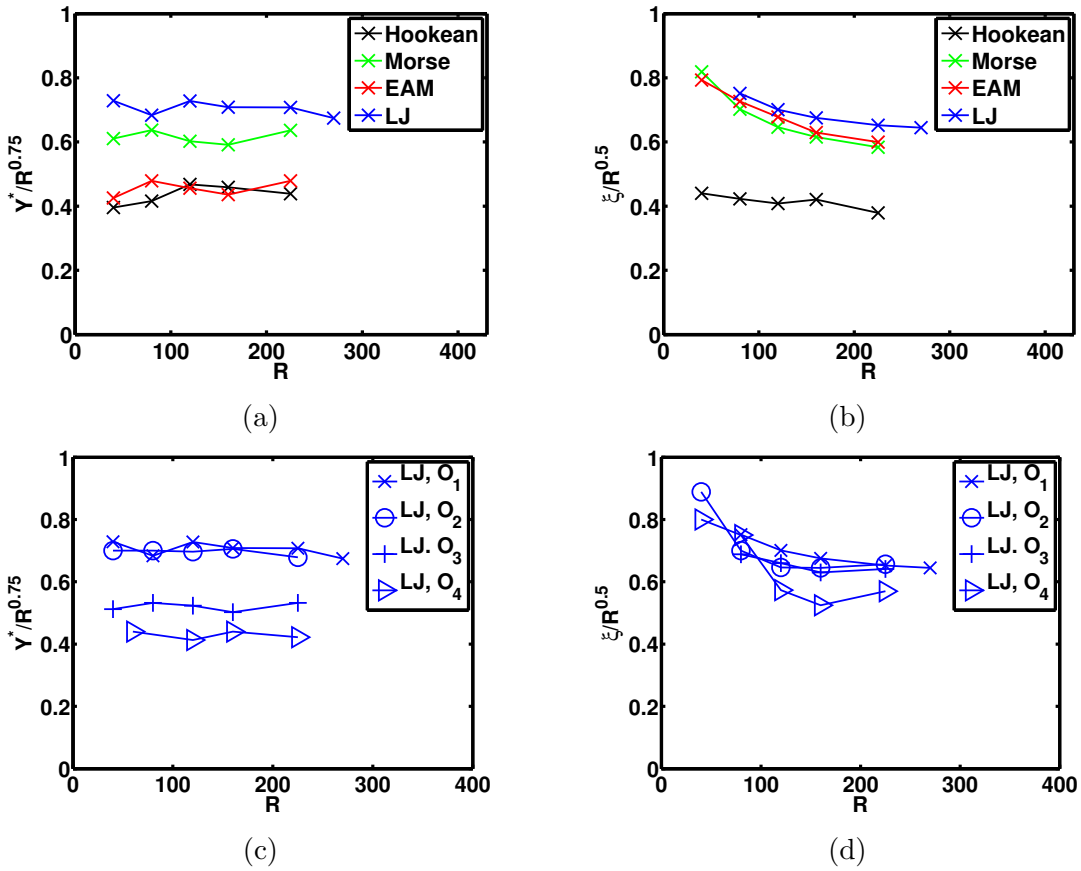

Figure 2.12: (a) Embryo center depth, Y^*, scaled by $R^{0.75}$ (b) Embryo size, ξ, scaled by $R^{0.5}$ - as a function of R for different orientations and interatomic potentials.

Y^*, and the embryo size, ξ. Both were also found to be roughly independent of L as shown in fig. 2.11 for LJ-O_1. We observe the following scaling laws for Y^* and ξ.

$$Y^* \sim\propto R^{0.75} \; or \; \frac{Y^*}{R} \sim\propto R^{-0.25} \tag{2.9}$$

$$\xi \sim\propto R^{0.5} \; or \; \frac{\xi}{R} \sim\propto R^{-0.5} \tag{2.10}$$

These scaling laws are essentially independent of interatomic potential and crystallographic orientation as shown in fig. 2.12. In the limit of large R despite the R independence of F_c/R and C_c/R, ξ/R and Y^*/R display non-trivial scaling with R. If R is the only relevant length scale, then any linear continuum description cannot explain these scaling laws. This implies that even though the linear elastic calculation is close to the actual F vs. C curves the non-linear behavior of material is important for explaining these non-trivial scaling laws for ξ/R and Y^*/R. In table 2.1, we show hardness, Fc/R, and embryo-size, ξ, for various orientations and inter-atomic potentials. The exact form of the mathematical relation between Fc/R and ξ is not clear, but the trend is clear - bigger embryo implies smaller hardness. For instance, LJ-O_4 is the hardest and has the lowest ξ among all orientations. As intuitively expected, among all potentials Hookean-O_1 is the hardest and has the lowest embryo size.

Table 2.1: $\xi/R^{0.5}$ and F_c/R for different potentials and orientations, $R > 100$

	LJ-O_1	LJ-O_2	LJ-O_3	LJ-O_4	EAM-O_1	Morse-O_1	Hookean-O_1
$\frac{\xi}{R^{0.5}}$	0.66	0.65	0.64	0.57	0.60	0.58	0.38
$\frac{F_c}{R}$	0.05	0.056	0.061	0.1	0.052	0.049	0.33

2.5 Λ criterion

Another question that has been investigated by many authors before is, whether it is possible to *predict* the onset of instability for HDN using a criterion? As shown in fig. 2.5a, the instability process involves a cluster of atoms (10 to 20 atoms) and is inherently non-local. Therefore, it is still not fully understood if this instability can be predicted by a locally measurable threshold criterion . The first naive local-criterion proposed was based on Maximum Resolved Shear Stress (MRSS) or Schmid factor. The resolved shear stress, τ, can be calculated using the projection, of the component of atomic-level shear stress on the critical plane, along the slip direction. The naive expectation is that the dislocation loop will nucleate at the location of τ_{max}, when τ exceeds the source threshold characteristic of the material. The maximum resolved shear stress (MRSS) calculated for LJ Potential, O_1 and O_4 is shown in fig. 2.13. Clearly, the MRSS does not predict the location of embryo accurately, as already shown by Kelchner [1].

Later, Li, VanVliet and co-workers formulated another local criterion, the Λ criterion [8] [15] [13]. Λ is based on Hill's analysis of the stability of plane waves in a homogeneously deformed crystal. $\Lambda_{\mu\nu}\{\vec{k}\}$ is the acoustic tensor. It is related to the dynamical matrix which gives the vibrational frequencies of phonons of a given

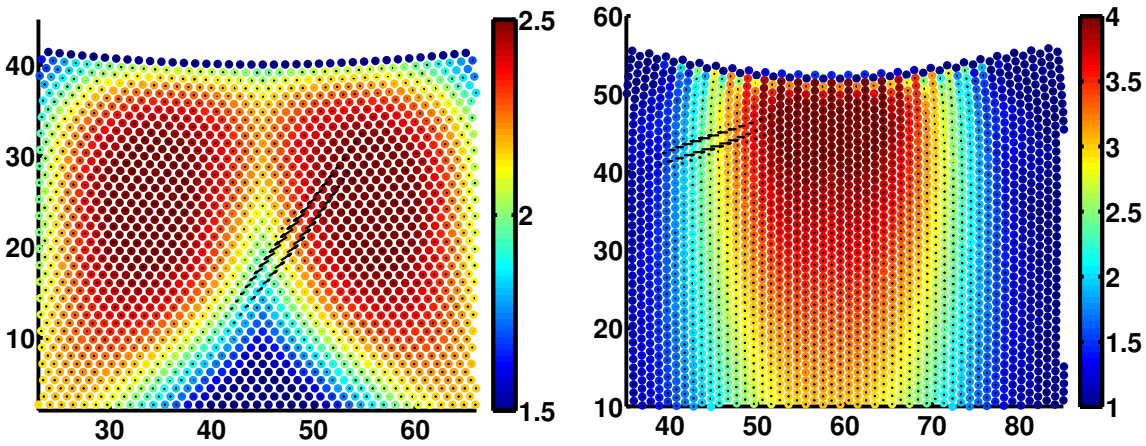

(a) LJ Crystal, O_1 orientaion (b) LJ Crystal, O_4 orientaion

Figure 2.13: Maximum resolved shear stress for each atom in LJ crystal, O_1 and O_4.

wavevector. $k^2\Lambda_{min}$ is then the lowest squared phonon frequency for the phonon of given wavevector. A negative value of Λ_{min} indicates an unstable phonon mode.

Λ is a function of local strain, which can be computed through several approaches, given the atomic positions in the crystal. We describe here two methodologies for local strain calculation, and for both cases our results are almost the same. One can define the local strain on each triangle in a 2D hex lattice using linear interpolation, as the strain was computed during the calculation of Ω in section 2.3. For each atom, the local strain is the algebraic average of the strain of six triangles around the atom. We also computed Λ for each triangle, instead of each atom, based on the strain in each triangle and the results were also almost the same in this case. The other procedure to calculate local strain is as done by Falk and Langer in [23] (see Appendix B). In this case, the local strain for an atom is the best fit uniform strain calculated using the nearest neighboring atoms. The acoustic tensor is defined for an

infinite homogeneously deformed lattice. Given the local deformation gradient, F, at particle, a, the initial lattice is homogeneously deformed. The dynamical matrix, D_{uv}, for the can be computed as:

$$D_{uv}(\vec{k}) = \sum_j H_{uv}(\vec{R_{aj}}) * e^{-i\vec{k}.\vec{R_{aj}}} \tag{2.11}$$

where, $\vec{R_{aj}}$ is the displacement vector defined from the local position, R_a, to the neighboring particle, j, in the homogeneously deformed crystal. H_{uv} contains the elements of the hessian matrix for a homogeneously deformed crystal as described in Appendix A. Equation 2.11 can be simplified to:

$$D_{uv}(\vec{k}) = \sum_j H_{uv}(\vec{R_{aj}})(cos(k\hat{k}.\vec{R_{aj}}) - 1) \tag{2.12}$$

Using the long wavelength approximation,

$$\begin{aligned} D_{uv}(\vec{k}) &\approx \sum_j -0.5 * H_{uv}(\vec{R_{aj}}) * (k\hat{k}.\vec{R_{aj}})^2 \\ &\approx (k^2) * \sum_j -0.5 * H_{uv}(\vec{R_{aj}}) * (\hat{k}.\vec{R_{aj}})^2 \end{aligned} \tag{2.13}$$

$$\Lambda_{uv} = \frac{1}{k^2} D_{uv}(\vec{k}) \tag{2.14}$$

For particle a, Λ is the minimum eigenvalue of Λ_{uv} over all $\vec{k}$.

Λ for EAM and LJ potentials for the stable surface orientation, O_1, and the unstable surface orientation, O_4, is shown in fig. 2.14. Note that Λ becomes negative before

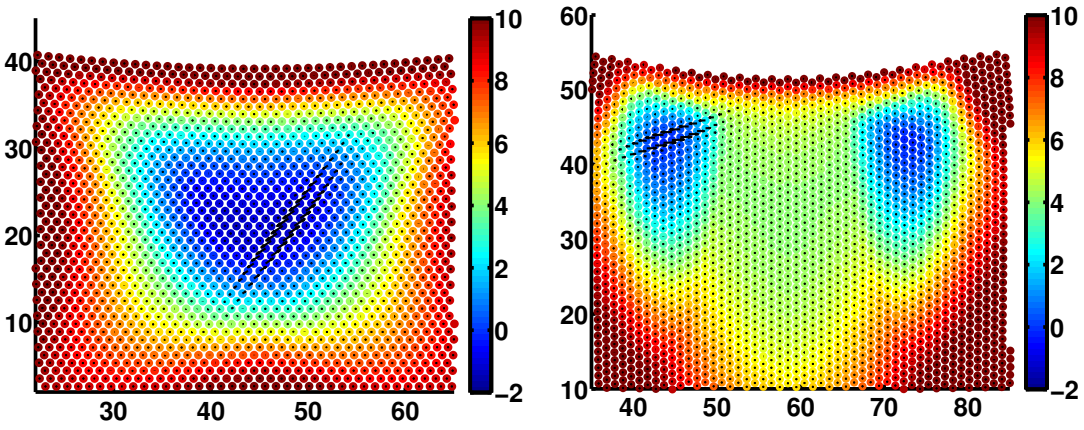

(a) LJ Crystal, O_1 orientaion

(b) LJ Crystal, O_4 orientaion

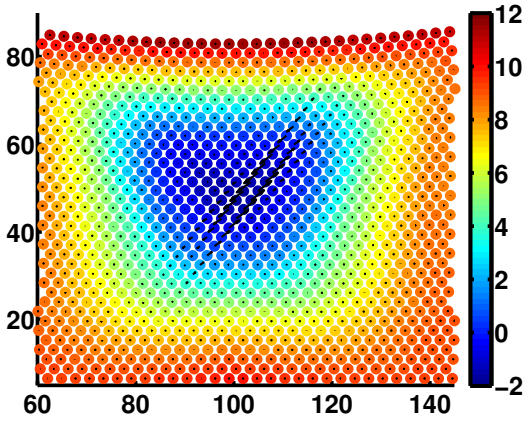

(c) EAM Crystal, O_1 orientaion

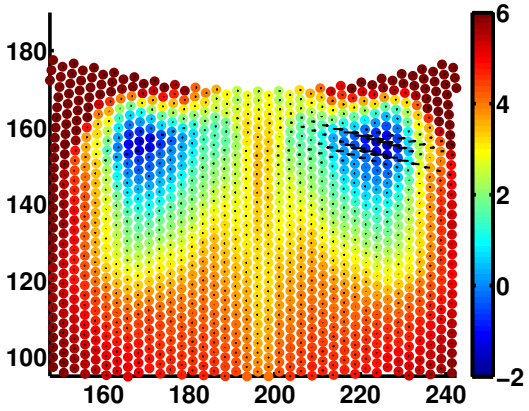

(d) EAM Crystal, O_4 orientaion

Figure 2.14: Minimum Λ value for each atom in LJ and EAM crystal, O_1 and O_4.

instability, this makes a strict correspondence between loss of stability and $\Lambda < 0$ untenable. Recently, MR [10] also showed that Λ becomes negative before the actual instability. Furthermore, they observed that Λ_{min} does not correspond to the embryo location for EAM-O_4. On the contrary, we always observe that Λ is minimum at the center of the embryo irrespective of the crystal orientation and the inter-atomic potential.

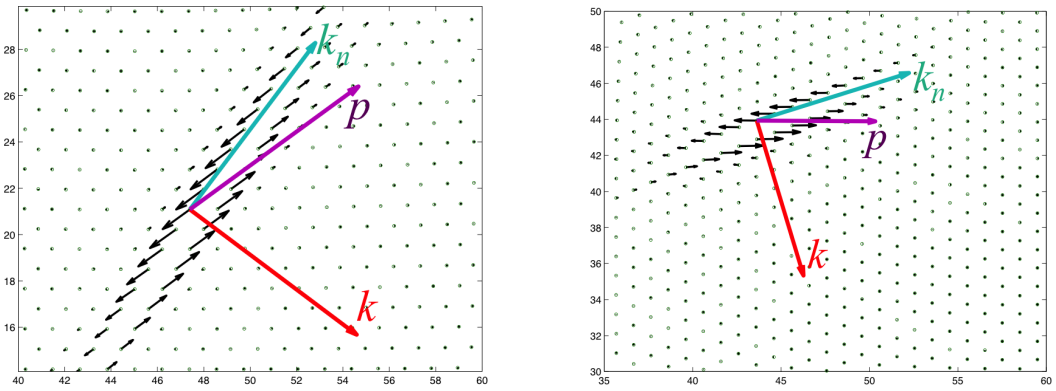

(a) LJ Crystal, O_1 orientaion (b) LJ Crystal, O_4 orientaion

Figure 2.15: Wavevector direction, $\hat{k}$; Normal to wavevector direction, $\hat{k_n}$; Polarization vector direction, $\hat{p}$ corresponding to minimum Λ in LJ Crystal for (a): O_1, (b): O_4.

In fig. 2.15 we also show the wave-vector, k, and the polarization vector, p, corresponding to the least stable phonon, for the atom with minimum Λ. As shown, the wave-vector, k, is almost perpendicular to the slip plane. The eigenvector corresponding to the minimum eigenvalue of Λ_{uv} or the polarization direction, p, is not perpendicular to the wave-vector, k; it is very close to the slip direction. These results are consistent across all crystal orientations and inter-atomic potentials.

2.6 Discussion and Summary

We have performed quasi-static simulations of homogeneous dislocation nucleation in the *bulk* of 2D hexagonal crystals for various orientations and interatomic potentials. For all orientations and interatomic interactions discussed in this chapter, we observe nucleation of a dipole of shear dislocations. The critical parameters: scaled critical

indenter load, F_c/R, and scaled critical contact length, C_c/R, become independent of R for large R values. However, the scaled size of embryo, ξ/R, and the scaled depth of embryo, Y^*/R, show non-trivial scaling with R even for large R values. These scaling laws are consistent for different interatomic interactions and lattice orientations. On simple dimensional grounds, no continuum theory containing only R as geometrical parameters can predict these scaling laws, to describe the embryonic location and size scaling. These scaling laws also need to be verified in macro-scale models inherently using interatomic potentials (as used in, e.g., reference [8]).

We also show dislocation nucleation for a *Hookean* crystal with perfect linear springs. The scaling laws are also robust for this Hookean crystal. This implies that the instability is *intrinsically geometrical*. However, the dependence of prefactors in the scaling laws on interatomic interactions and lattice orientations indicates some importance of non-linear material behavior in homogeneous dislocation nucleation.

One of the criticisms associated with Λ given by MR was that it becomes negative before instability nucleation. We concur with MR that Λ cannot be used as a nucleation criterion in this sense. However, Λ is always minimum at the center of embryo and it predicts the mode and the slip-plane accurately irrespective of the crystal orientation and interatomic potential. Therefore, Λ is much more useful than our expectations from the previous analysis by MR.

In this work we used a featureless infinite rigid indenter. In nano-indentation experiments one typically uses an indenter with a finite stiffness. For direct comparisons with experiments, the affect of indenter interaction with the substrate needs to be

understood carefully.

Finally, the role of temperature for the scaling of energy barriers also has to be studied. The energy barrier in the saddle node bifurcation mechanism of dislocation nucleation is dependent on temperature and other macro-scale properties such as indenter radius, R. This interdependence needs to be understood, to predict the hardness at finite temperature.

Chapter 3

Meso-scale analysis of homogeneous dislocation nucleation

3.1 Introduction

In perfect crystals the onset of plasticity is indicated by the events of dislocation nucleation. In microscale crystals, dislocations are typically produced by pre-existing defects in the material. However, in recent years, tools such as nanoindentation and the Atomic Force Microscopy (AFM) have allowed access to mechanical properties in nanoscale samples where one can obtain practically defect-free crystals. Therefore, homogeneous dislocation nucleation (HDN) during nano-indentation has been a matter of interest lately. Miller and Rodney (MR) showed that HDN is a meso-scale process involving tens of atoms forming an *embryo* underneath the indenter [10]. The importance of the non-local nature of this problem has also been emphasized in the work of Delph and Zimmerman for the development of Wallace criterion for the prediction of instability [24] [25]. The Wallace criterion is used for cavitation and crack growth problems in FCC solids. For HDN, Miller and Rodney (MR) developed a predictive criterion based on the meso-scale atomic acoustic tensor [10]. According to this criterion, HDN is indicated by loss of positive definiteness of the meso-scale acoustic tensor. The meso-scale criterion is similar to a previously proposed Λ criterion. Λ is a local quantity, calculated on an atom-by-atom basis [14] [2] [8] [9] . On the other hand, MR's criterion is based on the acoustic tensor of a cluster of atoms.

For the non-local analysis described by MR, one has to judiciously choose the meso-region for calculation of the acoustic tensor. MR did not discuss how the size and the location of the meso-region would affect the analysis. Maloney et. al. described the methodology for measuring the embryo size. They also showed that the embryo

grows in a non-trivial way with the radius of curvature of the indenter tip. An important question is what is the minimum size of the meso-region centered at the embryo required to capture the defect. We show here that even if the meso-region size is much smaller than the embryo, it can still reveal the instability. However, the meso-region captures the full spatial extent of the embryo only if the meso-region is bigger than the embryo.

Another important question we address in this work is: how far can the meso-region move from the embryo center to detect the instability? If the instability is local, one could naively assume that if the meso-region contains the minimum Λ location (i.e. the embryo center), it can predict the instability. However, our preliminary results contradict this. We determine the critical section of the embryo that the meso-region should necessarily contain to detect the instability. In this work, we also show that the meso-scale lowest eigenmode captures the embryo sooner than the full system eigenmode. This further highlights the utility of meso-scale analysis in terms of computational time and resources for atomistic simulations. We show that the meso-mode signals the instability, four to six orders of magnitude of distance (or load) to dislocation nucleation before the full system eigenmode.

The rest of this chapter is organized as follows. In section 3.2 we describe the details of our simulations and give a brief kinematic description of the mechanism of homogeneous dislocation nucleation. Section 3.3 contains our rationale and results on the meso-scale analysis. In particular, we discuss the significance of meso-region size by fixing the analysis at the center of embryo, and then vary the meso-region spatially and temporally. Section 3.5 concludes with a brief summary and discussion

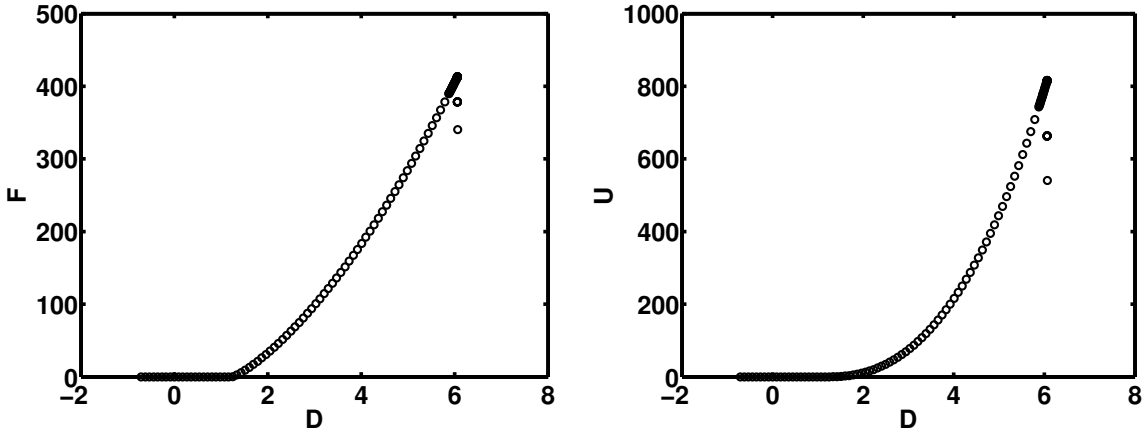

(a) (b)

Figure 3.1: (a) Elastic energy, U, stored in the crystal as function of indenter depth, D, LJ crystal, $L = 40$, $R = 40$. (b) Corresponding load, F, on the indenter in the vertical direction as function of indenter depth, D.

on implications of our results, together with outline of our future work.

3.2 Modeling and Eigenanalysis

We perform athermal quasi-static nano-indentation simulations for 2D hexagonal Lennard Jones crystals via energy minimization dynamics. The simulation methodology and kinematic analysis is described in sec. 2.2 and sec. 2.3. All energies and distances in this chapter are measured in Lennard-Jones units. The load-displacement and energy-displacement curves for the indentation process are shown in fig. 3.1. As shown in sec. 2.2, the system is driven to instability along a single eigenmode, that shows anti-parallel motion of small number of atoms on adjacent crystal planes, resulting in the nucleation of a dislocation dipole as shown in fig. 3.2b. In fig. 3.2a, the

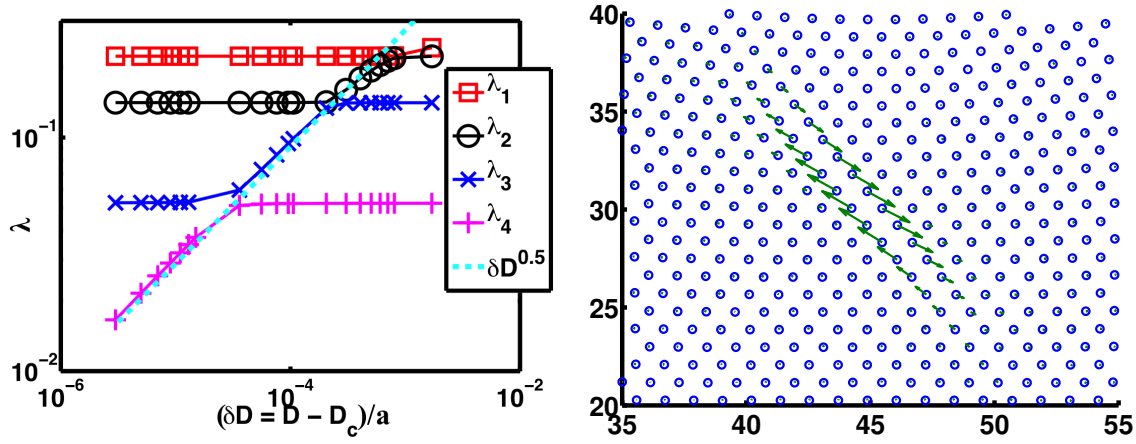

(a) (b)

Figure 3.2: Lowest 4 energy eigenvalues, λ, for $L = 160, R = 40$, O_1, LJ crystal, as function of $\delta D = D - D_c$. The cyan line is a critical energy eigenmode along which the system is driven to instability.

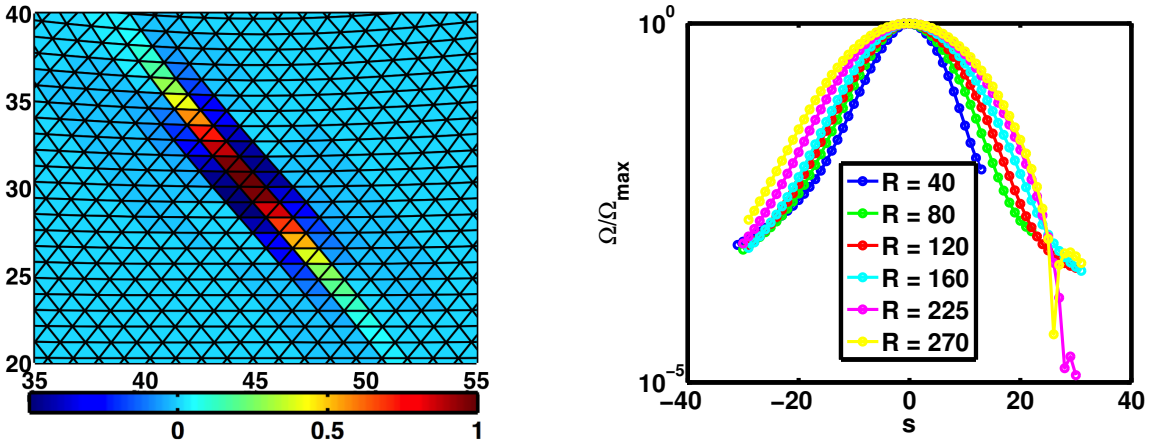

(a) (b)

Figure 3.3: (a) Lowest eigenmode at $\delta D = D - D_c \approx 10^{-6}$ for $L = 160$, $R = 40$, O_1, LJ crystal.
(b) Corresponding transverse mode gradient, Ω/Ω_{max}.

lowest eigenvalue, λ, of a critical meso-mode decreases with distance to dislocation nucleation, δD, as:

$$\lambda = a_1 * (\delta D)^{-0.5} \tag{3.1}$$

The calculation of Ω for computing the embryo size is given in sec. 2.3. Fig. 3.3a shows the Ω field corresponding to the mode shown in fig. 3.2b. Fig. 3.3b shows $\Omega(s)$ profiles for $L = 160$, $R = 40$.

3.3 Meso-scale Analysis of Incipient Dislocation

3.3.1 Rationale

As shown in the top panel of fig. 3.4, the lowest energy eigenvalue of an undeformed region scales as $1/r^2$, where r is the size of the meso-region. This is expected for an isotropic, linear, elastic 2D sheet of atoms in a crystal with fixed boundaries. The critical eigenmode for an undeformed region of radius, $r_{meso} = 8$, is a longwavelength mode as shown in the bottom left panel of fig. 3.4.

Just before nucleation, the critical eigenmode for a meso-region is localized as shown in the bottom right panel of fig. 3.4. The meso-region critical eigenmode, called meso-mode, looks similar to the full system eigenmode shown in fig. 3.2b. The lowest eigenvalue corresponding to the critical eigenmode falls off faster than any power law as shown by the curve in the top panel fig. 3.4.

A meso-region of radius as small as six interatomic distance can capture the defect

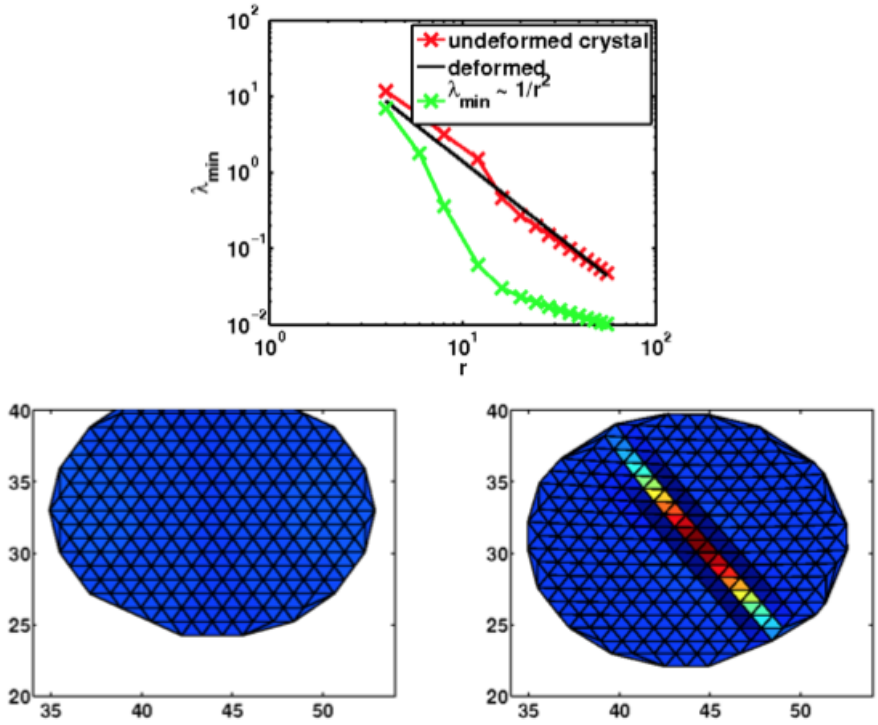

Figure 3.4: Top: Characteristic $\lambda_{min} \sim r_{meso}$ curves for an undeformed and a deformed crystal close to nucleation ($\delta D \sim 10^{-6}$). Bottom: Meso-region eigenmodes corresponding to the lowest energy eigenvalue of meso-region with radius $r_{meso} = 8$: from an undisturbed crystal (left) and a configuration close to dislocation nucleation (right).

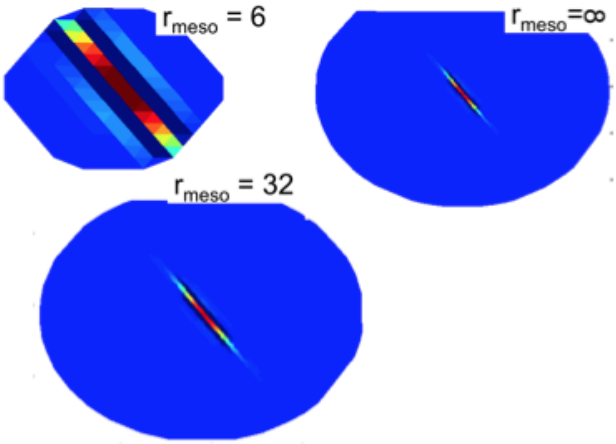

Figure 3.5: Structure of the meso-mode for 3 different r_{meso} from the system with $L = 160$, $R = 120$ and $\delta D \approx 10^{-6}$. $r_{meso} = \infty$ corresponds to the entire system. Note how quickly the meso-mode captures the structure of the incipient defect.

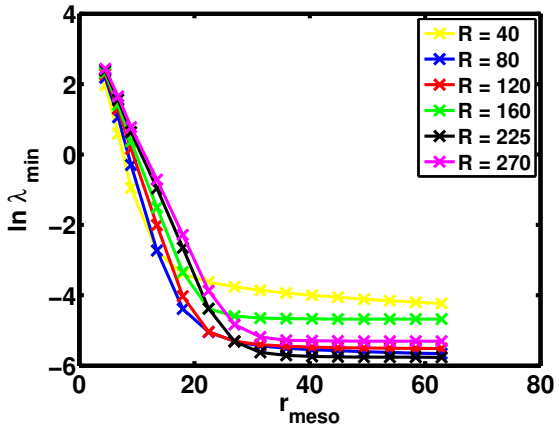

Figure 3.6: $\ln(\lambda_{min})$ versus r_{meso} curves for various indenter radii, R, and system size, $L = 160$.

as shown by the meso-mode in fig 3.5. Above a critical radius of the meso-region centered at the hot atom, the structure of the meso-mode saturates. In fig 3.5, the meso-mode for $r_{meso} = 32$ has the same spatial structure as the full system eigenmode. The energy of the meso-region, or the lowest eigenvalue initially decreases as the meso-region radius increases and then plateaus similar to the spatial structure of the meso-region. Fig. 3.6 is a log-lin plot for the meso-region eigenvalue vs. r_{meso} for different R. The height of the plateau is not function of R, it is governed by the distance from nucleation, δD, for the meso-scale analysis. On the other hand, the structure of the localized meso-mode is independent of the proximity to nucleation. Therefore, the rest of this work is focused on the structure of the meso-mode versus the eigenvalue associated with the meso-region.

3.3.2 Meso-Region centered at the Hot atom

We compute the eigenmode corresponding to the lowest energy eigenvalue, called meso-mode, for various r_{meso} with meso-regions centered at the embryo. Fig. 3.5 shows the meso-mode corresponding to $r_{meso} = 6$ and $r_{meso} = 32$ for $L = 160$, $R = 120$ and the critical portion of the eigenmode for full system($r_{meso} = \infty$). The $\Omega(s)$ profiles corresponding to these modes is shown in fig. 3.7. The width of the Ω curve for $r_{meso} = 8$ is smaller than that of the full system. The Ω curves converge when r_{meso} is greater than a critical value. As expected, they converge for $r_{meso} \gtrsim \xi$, however meso-regions smaller than ξ definitely have information about the inicipient instability.

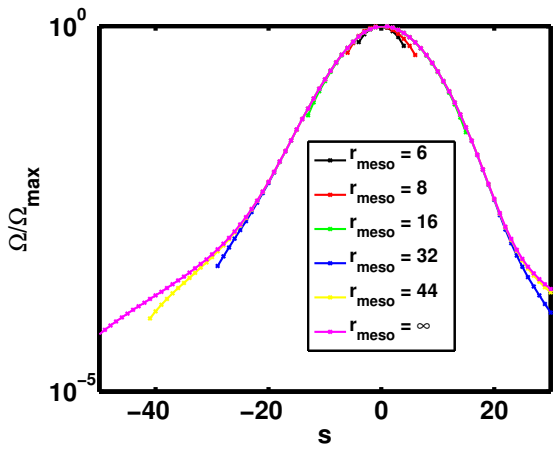

Figure 3.7: $\Omega(s)$ curves on slip plane computed from lowest eigenmodes of various meso-scale regions for R = 120, L = 160.

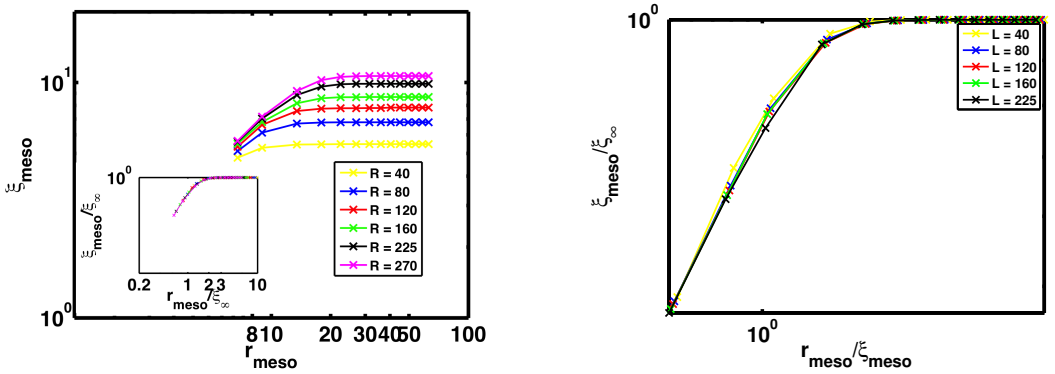

(a) (b)

Figure 3.8: (a) ξ_{meso} as a function of r_{meso} for various indenter radii, R and system size, $L = 160$. Inset shows that the curves can be made to collapse by rescaling the axes with their plateau value ξ_∞. (b) Collapsed ξ_{meso} versus r_{meso} curves (rescaled by ξ_∞) for indenter radius, $R = 160$ and different system sizes, L.

We next measure the spatial extents, ξ_{meso}, of the meso-region eigenmodes for all our systems. ξ_∞ is the spatial extent obtained from the full system eigenmode. Fig. 3.8a, shows $\xi_{meso} \sim r_{meso}$ for different indenter radii. As expected from fig. 3.8a, for small r_{meso}, ξ_{meso} increases before plateauing at ξ_∞. The increase of ξ_{meso} with r_{meso} for meso-regions smaller than ξ_∞ follows a power law. The insets shows the collapse of these curves when rescaled by their corresponding plateau value: ξ_∞. The collapsed rescaled curve in fig. 3.8b is universal for all indenter-crystal geometries. The fact that the plateauing of ξ_{meso} is seen for $r_{meso} > \xi_\infty$ can be reasonably expected from the fact that those meso-regions completely encompass the incipient dislocation.

The power law scaling of ξ_{meso} strongly suggests that for r_{meso} *smaller* than ξ_∞, the spatial structure of the lowest meso-mode does reveal the structure of the critical mode. However, for meso-regions of radius of one or two particle spacings the meso-mode invariably ceases to have the structure typical of an incipient dislocation. This scenario, where we can pick up the signature of an incipient dislocation with meso-regions smaller than its spatial extent - but not too small, indicates that homogeneous dislocation nucleation is a *quasi-local* phenomenon.

3.3.3 Meso-scale analysis centered off from the highest Ω triangle

In this section, we analyze the lowest eigenmode for the meso-region, called *meso-mode*, when the meso-region is not centered at embryo center. We define *critical meso-mode* as the mode that contains the signature of an incipient dislocation. In

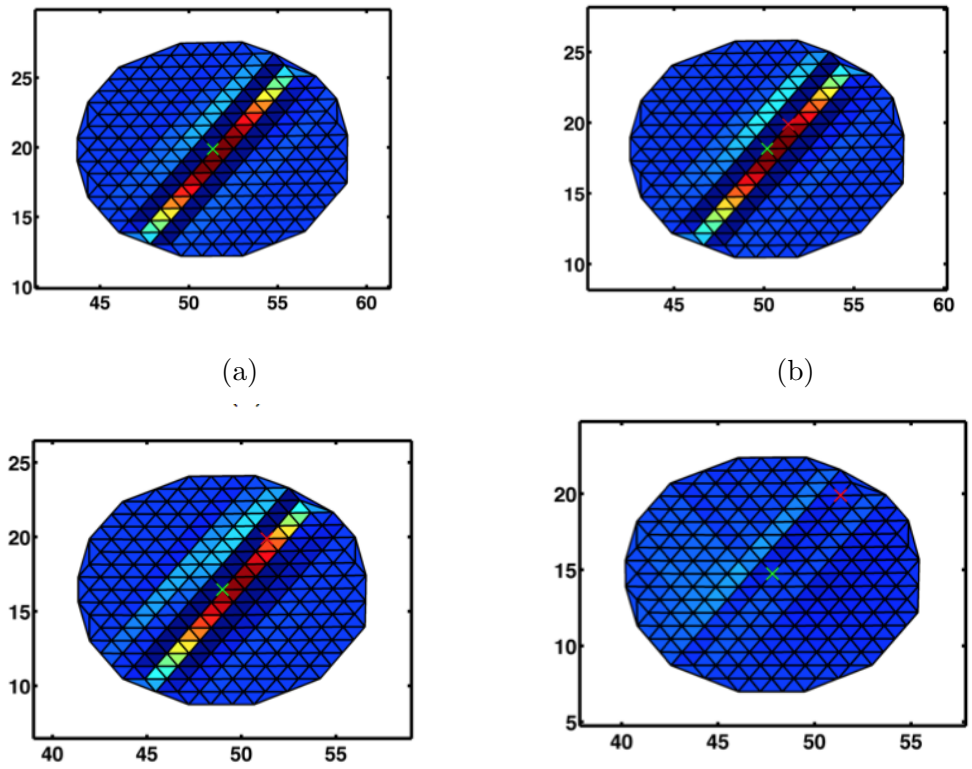

Figure 3.9: Structure of the lowest energy eigenmode for $r_{meso} = 8$ and indenter radius, R = 40 when the meso-region is moved along the slip plane. The 'red cross' corresponds to the embryo center and the 'green cross' corresponds to the meso-region center.

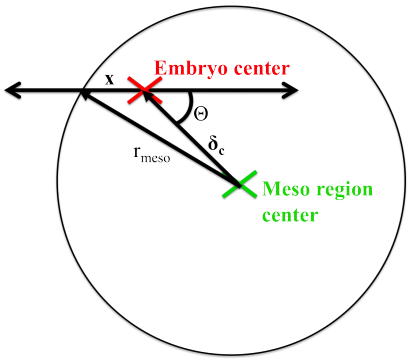

Figure 3.10: Schematic diagram used to derive the geometrical relation between δ_c, r_{meso} and x as in eq. 3.2. δ_c is the critical distance from the 'Hot atom' upto which the critical meso-mode has a lower energy than the long wavelength mode. x is the critical portion of the embryo required to capture the defect.

fig. 3.9, the meso-mode is shown when the meso-region is moved spatially along the slip plane. Upto a critical distance, δ_c, the meso-mode is the critical meso-mode. At δ_c, the long wavelength mode has lower energy than the critical meso-mode and the critical meso-mode no longer remians the meso-mode. The important question we address here is: How δ_c varies with the radius of meso-region, r_{meso}, and the embryo size, ξ?

We perform meso-scale analysis centered at atoms around the embryo for different embryo sizes. In fig. 3.11, the size of the meso-region is fixed, $r_{meso} = 40$. The colors at each atom represent maximum Ω for the meso-mode. The meso-mode is found to be the critical meso-mode when the meso-region is centered on the red atoms. The area formed by the red atoms depends on r_{meso} and ξ.

Again, δ_c is the critical distance from the center of the embryo upto which the critical meso-mode has a lower energy than the long wavelength mode. If we assume that

the meso-region should contain some critical portion of the embryo as shown in the diagram 3.10, δ_c can be written as in eq. 3.2, where x is the critical portion of the embryo.

$$\begin{aligned} x + \delta_c cos\theta &= (r_{meso}^2 - \delta_c^2 sin^2\theta)^{0.5} \\ \delta_c &= -xcos\theta + r_{meso}(1 - x^2 sin^2\theta / r_{meso}^2)^{0.5} \end{aligned} \tag{3.2}$$

Assuming $r_{meso} >> x$,

$$\delta_c = r_{meso} - xcos\theta - (x^2 sin^2\theta)/(2r_{meso}) \tag{3.3}$$

Along the slip plane, for $\theta = 0$,

$$\delta_c = r_{meso} - x \tag{3.4}$$

To compute x, we move our meso-region along the slip plane for various r_{meso} and ξ as shown in fig. 3.12a. For $r_{meso} >> \xi$, x is constant with varying r_{meso} and increases with increase in ξ (or R). From fig. 3.12b, x is found to be 1.2 ξ. This value of x is substituted back in eq. 3.3. Then, in fig. 3.11 δ_c based on the eq. 3.3 is shown by the black curves for different R (or ξ). The black curves predict the area formed by red atoms fairly well. This implies, if $r_{meso} > \xi$ then it must encompass roughly 120% of ξ to be the critcal meso-mode.

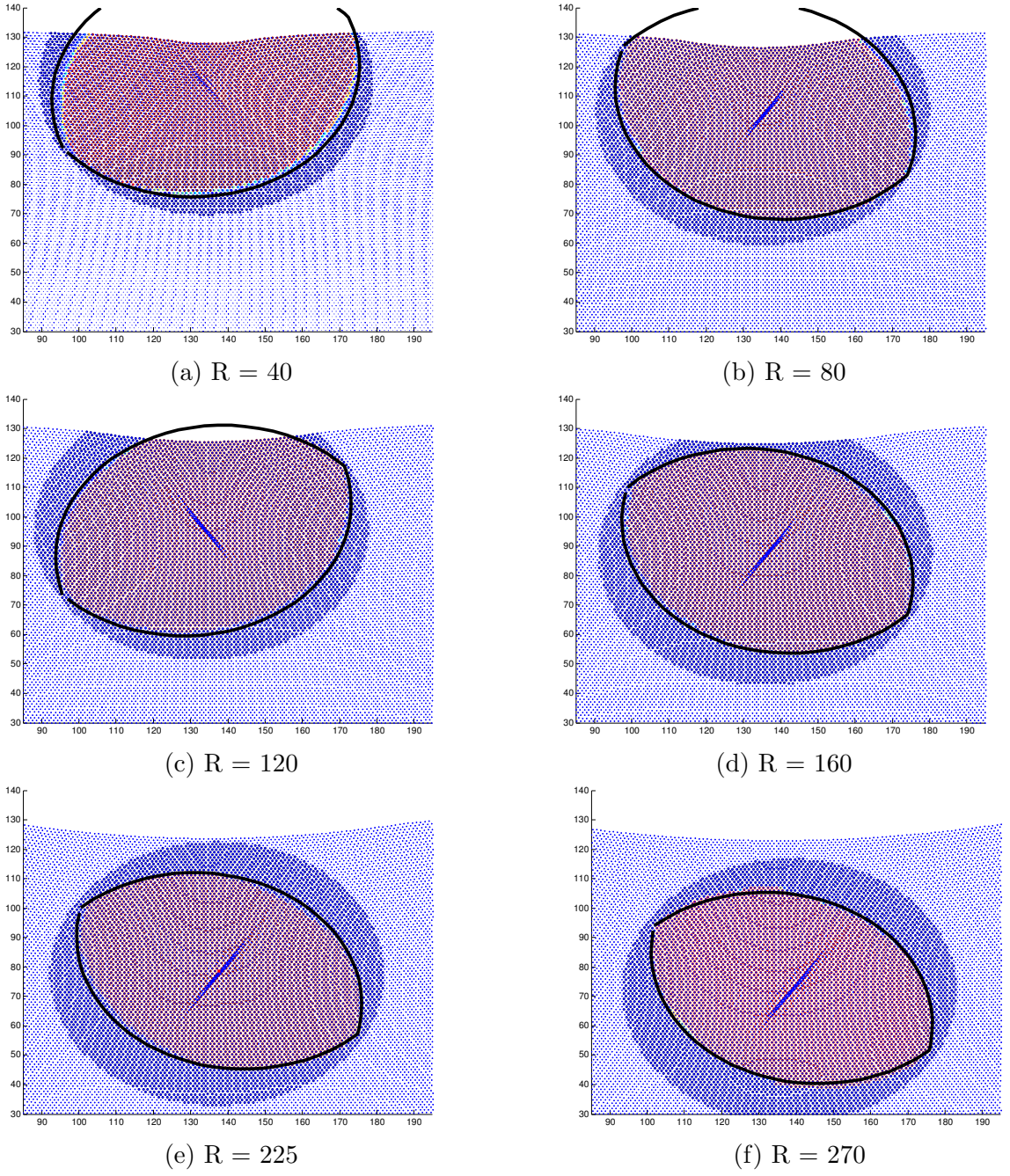

(a) R = 40 (b) R = 80

(c) R = 120 (d) R = 160

(e) R = 225 (f) R = 270

Figure 3.11: For fixed $r_{meso} = 40$ and various indenter radius, R when the meso-region is centered at the 'red' atoms, the lowest mode can detect the embryo. The colors represent maximum Ω for the lowest mode. The black curve shows the prediction based on the eq. 3.3 for δ_c.

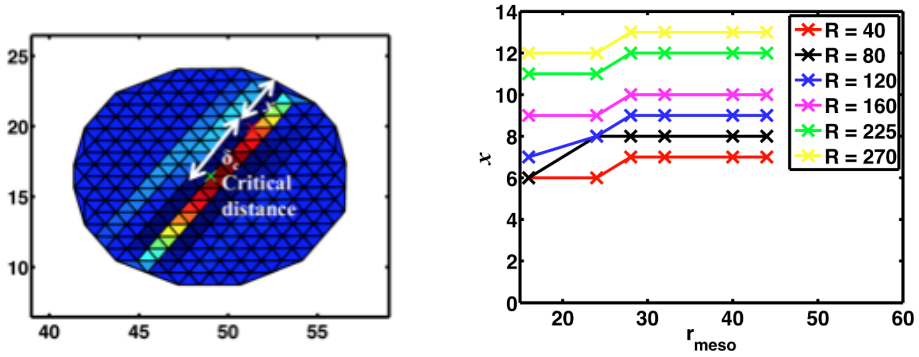

(a) (b)

Figure 3.12: Analysis when the meso-region is moved along the slip plane. (a): Schematic diagram for eq. 3.4 (b): x, the portion of embryo necessary for the lowest mode to be the critical mode vs. r_{meso} for different indenter radii, R.

3.3.4 Meso-scale analysis away from nucleation (temporally)

Here, we address: At what critical indenter depth, δ_D, the meso-mode becomes localized. In other words, at what δ_D or δ_F, does the energy of the critical meso-mode becomes lower than the long wavelength meso-mode. We study the dependence of δ_D with r_{meso}. Before nucleation as shown in fig. 3.2a, the lowest eigenvalue, λ, of a critical meso-mode decreases with distance to dislocation nucleation, δD, as:

$$\lambda = a_1 * (\delta D)^{-0.5} \tag{3.5}$$

In section 3.3.1, it was described that the eigenvalue corresponding to the long-wavelength meso-mode, λ_e, is a function of size of the meso-region, r_{meso}, given by:

$$\lambda_e = a_2 * (r_{meso})^{-2} \tag{3.6}$$

At critical distance, δ_D, or critical indenter force, δ_F, the energy of the critical meso-mode becomes equal to the long-wavelength mode energy. This gives the analytical relation between δ_D and r_{meso}:

$$\delta_D = a(r_{meso})^{-4} \tag{3.7}$$

We compute δ_D and δ_F vs. r_{meso} curves from simulations as shown in fig. 3.13. The power law derived in eq. (3.7) is also observed in simulations. δ_D vs. r_{meso} curves collapse when r_{meso} is scaled by intrinsic embryo size, ξ, and δ_F vs. r_{meso} collapse when r_{meso} is scaled by $\xi^{1.5}$. This can be derived from the fact that hardness, δ_F scaled by R, is the critical quantity equivalent to δ_D and ξ increases as a square root of R. From these curves it can be seen that, as the system size approaches infinity δ_D goes to zero. In other words, meso-scale analysis predicts nucleation much earlier than the full eigenmode analysis.

3.4 Scaling laws in fully three dimensional simulations using meso-scale analysis

We perform computational nano-indentation on a face-centered cubic (FCC) lattice using a spherical indenter of radius R as described in sec. 4.2.2. At each indenter step, the Hessian matrix is computed for the FCC lattice, similar to the two dimensional simulations. Diagonalization of the Hessian matrix for a three dimensional system can be computationally very expensive. Some of the systems considered for this

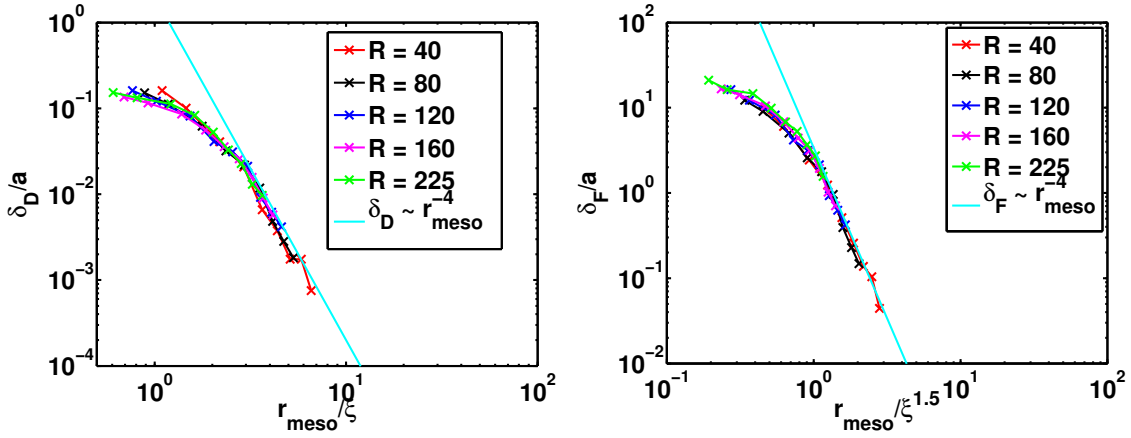

Figure 3.13: The critical time (required for the lowest mode to be the critical mode) measured from the bifurcation point, δ_t vs. r_{meso} for various indenter radius R.

work contain million atoms approximately. We use meso-scale analysis described in sec. 3.3 to compute the critical meso-mode. First, we measure the embryo size, ξ, and the embryo location, Y^*, for a smaller system size, L, and a smaller indenter radius, R, using full system kinematic analysis. Then the results for the smaller R are extrapolated to calculate ξ and Y^* for the required R, assuming $\xi \propto R^{0.5}$ and $Y^* \propto R^{0.5}$. These scaling laws for ξ and Y^* were obtained in chapter 2. Later in this section they are shown to hold true for the FCC lattice as well. Then we use very small meso-regions, $r_{meso} \approx 6$, close to Y^* to find the embryo. Following sec. 3.3.1 and sec. 3.3.2, it was seen that very small meso-regions, $r_{meso} \approx 6$, can capture the embryo. It was noted in sec. 3.3.3 that the meso-region not centered at the embryo can also capture the incipient dislocation. To search for the embryo, the meso-scale analysis was performed only once in each spherical zone of a radius of 6 atomic units. Since the meso-regions used were small, and the analysis was performed only at a

few locations, locating the embryo was computationally quick. Once the embryo was located, we used a meso-region of radius, $r_{meso} \approx 1.5\xi$, centered at the embryo to capture the structure of the critical eigenmode. We utilized the result obtained in sec. 3.3 that $r_{meso} \approx \xi$ is needed to capture the structure of the embryo. It was verified that increasing r_{meso} does not change the results.

The critical meso-mode for $L = 65$ and $R = 65$ is shown in fig. 3.14. At the onset of instability, there are two planes slipping with respect to each other resulting in the nucleation of a dislocation loop. The critical slip plane is (111) and the slip direction is $< 121 >$. As shown, the embryo structure located on (111) is hexagonal. We triangulate (111) plane containing the embryo using Delaunay triangulation. Each triangle and the vertex atom on the adjacent plane forms a tetrahedron. The critical meso-mode is interpolated on these tetrahedrons using linear finite element shape functions. Using this interpolation, Ω is defined as the curl of the critical meso-mode resolved in the direction perpendicular to the slip plane, as done in sec. 3.2 for the two dimensional simulations.

We call the three diagonal axes of the hexagonal embryo as n_1, n_2 and n_3, as shown in fig. 3.15. Ω vs. s is plotted in fig. 3.15 to obtain the embryo size (as done in sec. 3.2). Interestingly, the Ω vs. s curves along the three diagonal axes collapse, implying that the embryo is regular hexagon. The collapse of these curves was observed for all indenter radii. The embryo size, Ω, can be calculated from these Ω vs. s curves by fitting Gaussian profiles as done in sec. 3.2.

We observe the following scaling laws for the embryo location, Y^*, and the embryo

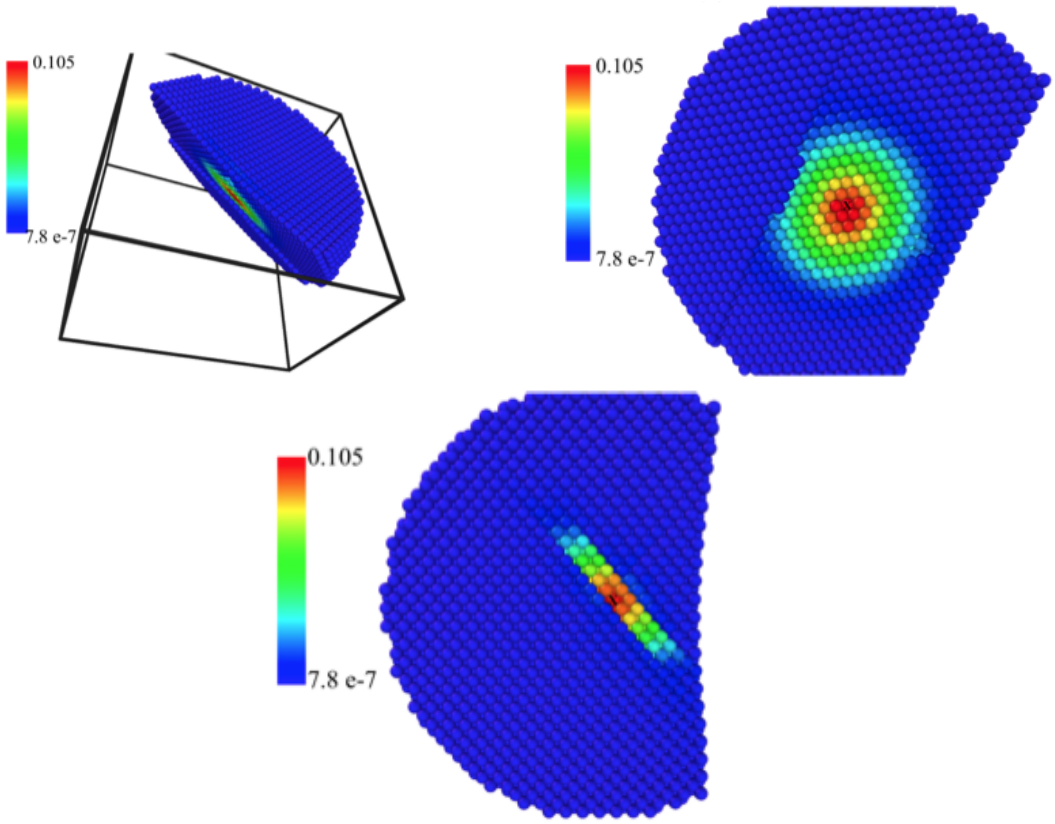

Figure 3.14: Critical meso-mode centered at the embryo core. Different views of the embryo are shown. The colors show magnitude of the mode at each atom.

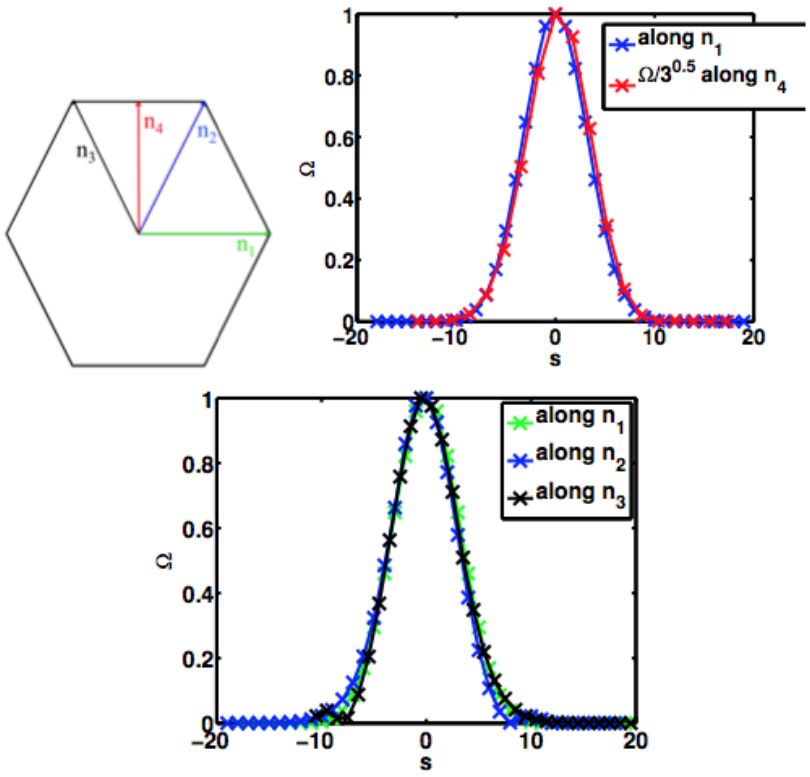

Figure 3.15: Top: Ω vs. s along n_1 and n_4. Bottom: Ω vs. s along n_1, n_2, n_3.

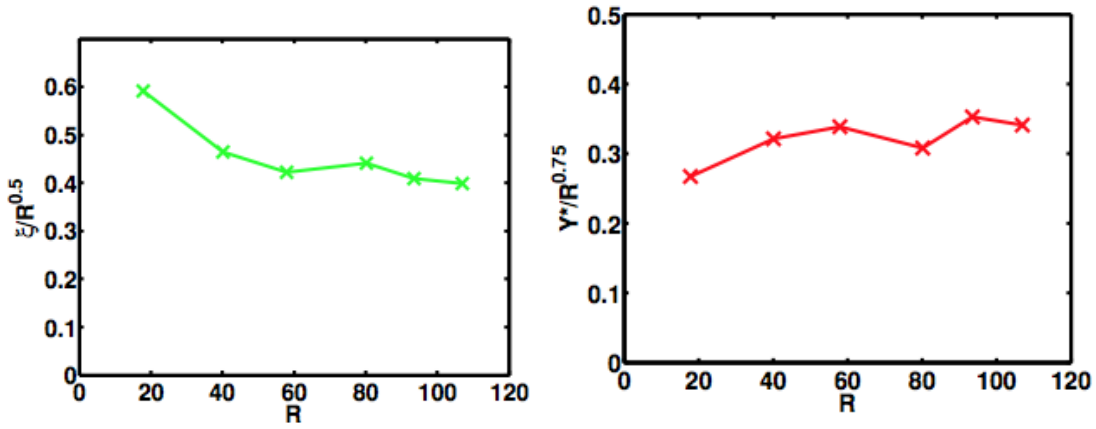

Figure 3.16: Left: The embryo size, ξ, scaled by $R^0.5$ as a function of R. Right: The embryo core depth from the surface, Y^*, scaled by $R^0.75$ as a function of R.

size, ξ (fig. 3.16).

$$Y^* \sim\propto R^{0.75} \; or \; \frac{Y^*}{R} \sim\propto R^{-0.25} \tag{3.8}$$

$$\xi \sim\propto R^{0.5} \; or \; \frac{\xi}{R} \sim\propto R^{-0.5} \tag{3.9}$$

These scaling laws are consistent with two dimensional simulations. These scaling laws were shown to be independent of interatomic potentials and crystal orientation for two dimensional hexagonal crystals. Similar to the two dimensional hexagonal lattice, for FCC L-J lattice, ξ/R and Y^*/R display non-trivial scaling with R despite the R independence of hardness and indentation size effect is observed for small R.

3.5 Discussion and Summary

In this chapter, we studied the nucleation of dislocation dipoles in the bulk of perfect 2D crystals subjected to nanoindentation with a circular, atomistic indenter under athermal, quasistatic conditions. We performed meso-scale analysis of configurations at the stability threshold, showing that small, non-local regions of the crystal, centered at the embryo, contain significant information about an incipient nucleation event. However, unlike previous work that utilized the minimum eigenvalue of the meso-regions as the main analysis tool [10] [24] [25], we focused our attention on the spatial structure of the lowest meso-region eigenmode. We found that the relation between ξ_{meso}, the embryonic size inferred from the meso-region, and r_{meso}, the size of the meso-region itself is universal. The lowest meso-mode and eigenvalue were found to provide excellent estimates of the structure and energy of the true critical mode, but only for meso-regions larger than $r_{meso} > 1.5\xi$. We also showed that the meso-regions not centered at the embryo center also reveal the presence of embryo, provided they encompass 1.2ξ. This scenario leads us to think of homogeneous dislocation nucleation as quasi-local: full information about the nature of the embryo can only be obtained by analyzing sufficiently large regions, however, its existence can be inferred by examining regions much much smaller than its intrinsic size.

We have also understood the effects of the proximity to nucleation, δD, on meso-scale analysis. Meso-scale analysis detects the embryo presence much before that the full system kinematic analysis. Meso-scale analysis can be used to make simulations computationally very efficient, especially for 3-D simulations where full system

kinematic analysis could be challenging or, in some-cases impossible. We showed an initial study for fully 3-D FCC crystal nano-indentation simulations using the meso-scale analysis. The critical meso-mode was used to calculate the embryo size, ξ, and the embryo location, Y^*. ξ and Y^* vary as the square-root of indenter radius for 3-D FCC lattice. These scaling laws consistent with the two dimensional hexagonal lattice simulationsd for various interatomic potentials and crystal orientations..

The ultimate use of the analysis presented here would be to inform coarser-grained models, that do not explicitly take into account the atomic degrees of freedom, about the creation of new dislocations out of the void. For example, in field dislocation mechanics [27] [28] one introduces a continuous field to represent the dislocation density. It is our hope that a criterion for dislocation nucleation based on a meso-scale analysis like we presented here could serve as a guide for the introduction of atomistic details at the dislocation embryo in concurrent multi-scale schemes built on field theories like FDM.

Chapter 4

A study of conditions for dislocation nucleation in coarser-than-atomistic scale models

4.1 Introduction [1]

Homogeneous dislocation nucleation (HDN) has been studied experimentally [29] [30] [3] and through modeling in many papers. Attempts have been made to formulate a nucleation criterion [9] [5] [8] [10] that can be used in larger length-scale analysis to predict the nucleation event. Ideally, the criterion should predict the precise location and instant of instability. It should also be able to predict the line direction and the Burgers vector associated with the nucleating dislocation loop. The simplest attempt to predict nucleation was based on atomic level shear stress, called Schmid stress, which was proven insufficient, when tested through numerical simulations. Rice and co-workers [31] [32] also proposed a nucleation condition for dislocation emission from crack tips, based on the notion of γ-surface given by Peierls and Nabarro [33] [34], and Vitek [35]. This γ-surface approach has been shown to be very useful in analysis of nucleation near crack tips [31] [32]. However, this approach fails qualitatively for homogeneous dislocation nucleation [10]. Li et al. [8] introduced the Λ criterion, which was based on Hill's analysis [14] of stability of plane waves in a deformed crystal. Miller and Acharya [5] proposed a stress gradient based approach to predict HDN.

Miller and Rodney (MR) [10] showed that while these criteria work well for certain interatomic potentials and indentation geometries, they fail qualitatively for others. Another fundamental question that was raised by MR is whether the instability is a local or a non-local process. They showed that HDN is inherently a non-local

[1] Sections 4.1, 4.4 and 4.6 were jointly written with Prof. Acharya and form parts of a paper submitted for publication. They are included here for completeness.

process because of the onset of collective floppiness. Supporting this argument, quantitative estimations of the size of the non-local unstable embryo were obtained in [36]. They also showed that Λ predicts the location of incipient nucleation in a diffuse region for HDN irrespective of the interatomic potential and orientation. However, Λ cannot predict the instant of nucleation. In this work, we review the previously proposed criteria - the Schmid stress, Λ criterion, Stress Gradient criterion and discuss their advantages and limitations. A major inadequancy associated with these criteria is that none of them predicts the instant of nucleation. MR [10] claimed that this is because of their inherently local nature. They also proposed a non-local criterion based on the calculation of eigenvalues of mesoscale atomistic stiffness matrix that precisely predicts the location and instant of nucleation. However, as acknowledged by them, it is not clear how MR's criterion can be extended to larger length scale Discrete Dislocation Dynamics (DD) or continuum analysis. In this work, we propose a technique based on linear stability analysis of the evolution equation for dislocation density in the finite deformation theory of Field Dislocation Mechanics (FDM) [27, 37, 38, 39]. While we evaluate it based on input from velocity fields calculated from atomistic simulations, the analysis naturally lends itself to application in self-contained continuum analysis including cases of non-homogeneous nucleation. The analysis uses the local velocity gradient field; however it is non-local in the sense that the velocity field is calculated using the boundary conditions, loading conditions and the overall stiffness matrix encapsulating non-local effects.

We validate the predictions of the linear stability analysis of FDM in both two-dimensional and fully three-dimensional simulations. We also examine this tech-

nique for different crystal orientations and interatomic potentials such as Embedded Atom Method (EAM) potentials for Al in addition to simple pair potentials such as Lennard-Jones. This analysis precisely predicts the location and instant of instability. In three-dimensional simulations, the nucleating dislocation density tensor lies in the linear span of critical eigenmodes predicted by the analysis based on FDM. Furthermore, we use a stress gradient criterion [40] to calculate the line direction for 3D simulations. Our results show that the stress gradient criterion predicts the line direction correctly for edge dislocations. However, for mixed dislocations the stress gradient criterion only predicts the edge component of the actual line direction. Interestingly, the proposed analysis discriminates between objective tensor rates; a naturally emergent convected rate succeeds while its substitution by a corresponding rate based on the skew part of the velocity gradient is shown to never predict nucleation.

A very simple overall physical picture emerges for our analysis of nucleation. At the atomistic level, dislocations are simply special arrangements of atoms, not immediately related to deformations of bodies and the compatibility of such deformations. Thus, FDM theory treats them as a special field, separate from a direct connection to the material motion. Special patterns of velocity fields defined on an atomic configuration give rise to the generation of the configurations we call as dislocated. As we explain in detail in this paper, our analysis of dislocation nucleation simply constitutes a detailed characterization of instantaneous velocity fields out of any attained configuration of the body (the whole set of atoms involved) that has the potential of generating configurations with dislocations. Interestingly enough, because of the

existence of the interatomic spacing between any two atoms, a velocity field defined from discrete atomistic velocities can almost always be considered as continuous, with its gradient being necessarily compatible. It turns out that it is precisely this compatibility of the velocity field that often plays a necessary role in being able to predict the nucleation of a dislocation, classically considered a *defect* or a lack of compatibility, as shown in section 4.4.

In section 4.2, we describe the modeling details and loading algorithm for different crystal orientations and interatomic potentials. In section 4.3, we review the Schmid stress, the Λ, and the Stress Gradient criteria. In section 4.4, we present the FDM linear stability based analysis of dislocation nucleation. In section 4.5, we discuss the results of this analysis for different orientations and potentials. Section 4.6 contains some concluding remarks.

4.2 Simulation Formalism

4.2.1 2 Dimensional Simulation

The simulation methodology for 2-D simulations is given in sec. 2.2. The load-displacement and elastic energy-displacement curves for the indentation process are shown in Fig. 4.1.

We look at two different orientations: O_1 and O_2 for our analysis as shown in Fig. 4.2. O_1 has the nearest neighbor axis aligned normal to the indenter motion axis. In

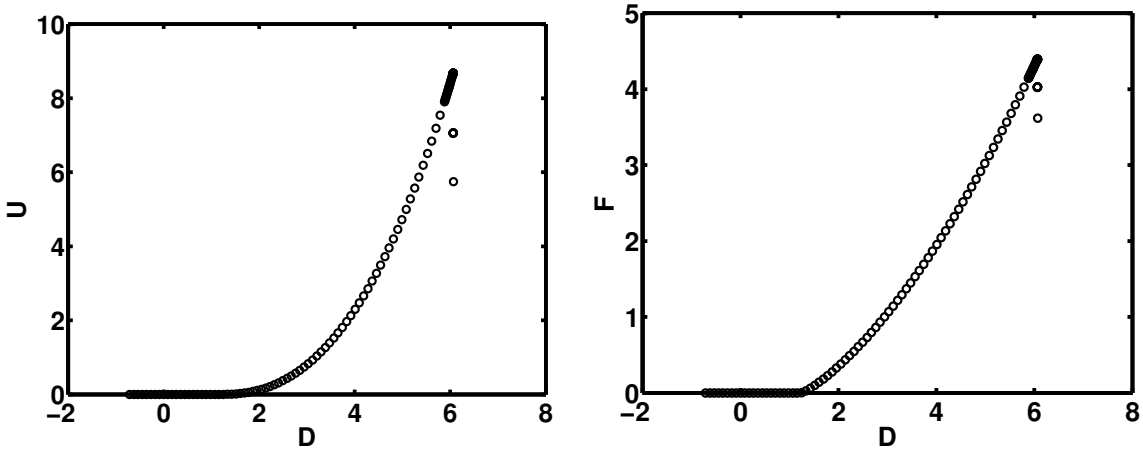

(a) (b)

Figure 4.1: (a) Elastic energy, U, stored in the crystal as function of indenter depth, D, L-J crystal, $L = 40$, $R = 40$. (b) Corresponding load, F, on the indenter in the vertical direction as function of indenter depth, D.

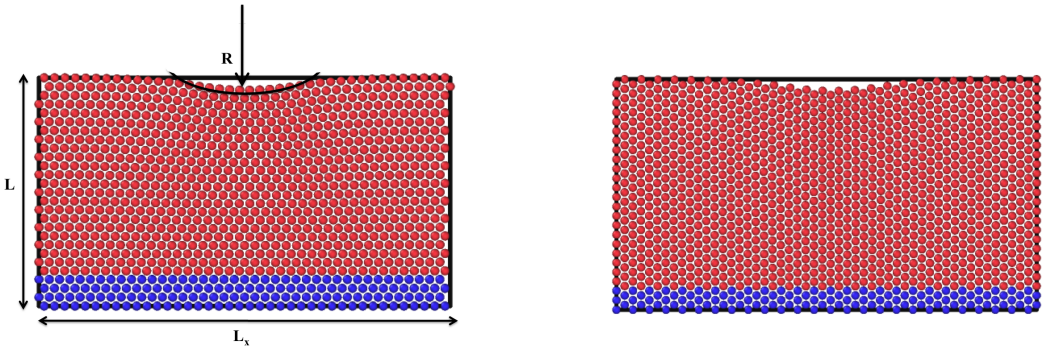

(a) (b)

Figure 4.2: Schematic of different orientations of crystal with respect to indenter axis. The red atoms correspond to the crystal and the blue atoms correspond to the rigid base a) O_1 b) O_2.

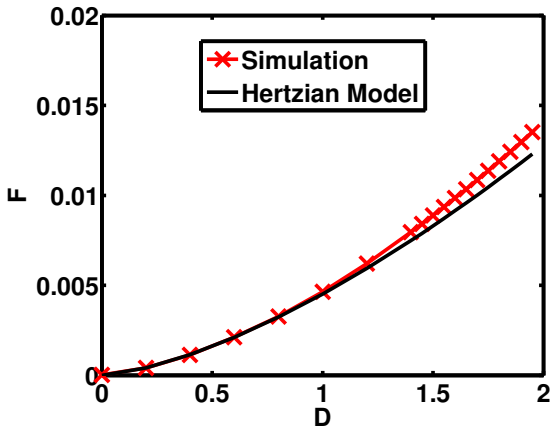

Figure 4.3: Indenter Load, F, as a function of indenter depth, D, for $L = 65$, $R = 65$. F vs. D curve from the simulation has been compared to the Hertzian analytical expression $F \propto D^{3/2}$.

O_2 the nearest neighbor axis is parallel to indentation direction. O_2 is the highest surface energy orientation, hence we had to be careful in avoiding surface defects while indenting these high surface energy orientation systems. In the rest of the document length parameters: L_x, L, R and C are measured in units of the lattice constant, a.

We use the Lennard-Jones (L-J) potential and the EAM potential for Al (Ercolessi Adams [18]). The Lennard-Jones (L-J) interaction potential is a pair-potential of the form;

$$U'(x_{ij}) = \epsilon((\sigma/x_{ij})^{12} - (\sigma/x_{ij})^{6}). \tag{4.1}$$

Here ϵ and σ set the energy and the length scales, and we set them equal to unity. x_{ij} is the distance between particle i and j. We also validate the results for both the orientations O_1 and O_2. The total potential energy, U, includes interatomic potential

energy between particles and interaction energy due to the indentor i.e.

$$U = \sum_{ij, i \neq j} U'(x_{ij}) + \sum_{i} \phi(r_i), \tag{4.2}$$

where r_i is $r_i(x_i, D)$. Latin characters are used to index particle number, and Greek characters to index Cartesian components. The indenter depth, D, represents the indenter motion towards the crystal. At each indenter step, we compute the Hessian matrix, which is the second derivative of the total potential energy with respect to the particle positions,

$$H_{i\alpha j\beta} = \frac{\partial^2 U}{\partial x_{i\alpha} \partial x_{j\beta}}. \tag{4.3}$$

The first derivative of energy with respect to the particle position gives the force on each particle:

$$F_{i\alpha} = -\frac{\partial U}{\partial x_{i\alpha}}. \tag{4.4}$$

$\frac{\partial U(x, D)}{\partial x_{i\alpha}} = 0$ represents equilibrium assuming D is an externally prescribed degree of freedom. Then,

$$\frac{\partial^2 U}{\partial x_{i\alpha} \partial x_{j\beta}} \frac{dx_{j\beta}}{dt} = -\frac{\partial^2 U}{\partial x_{i\alpha} \partial D} \frac{dD}{dt}. \tag{4.5}$$

The rate of change in forces with respect to the motion of the indenter is denoted by:

$$\Xi_{i\alpha} = \frac{\partial F_{i\alpha}}{\partial D} = -\frac{\partial^2 U}{\partial x_{i\alpha} \partial D}. \tag{4.6}$$

Since D monotonically increases in time, t, (4.5) can be written as:

$$\frac{\partial^2 U}{\partial x_{i\alpha} \partial x_{j\beta}} \frac{dx_{j\beta}}{dD} = -\frac{\partial^2 U}{\partial x_{i\alpha} \partial D}. \tag{4.7}$$

The forces induced by an infinitesimal external indenter motion must be balanced by the internal atomic rearrangements as shown:

$$H_{i\alpha j\beta} \dot{x}_{j\beta} = \Xi_{i\alpha}. \tag{4.8}$$

This is used to calculate particle 'velocities' $\dot{x}_{j\beta} = \frac{dx_{j\beta}}{dD}$. The analytical expression of $H_{i\alpha j\beta}$ can be simply derived for pair potentials such as L-J potential using the following expression (4.9) from [20],

$$M_{i\alpha j\beta} = (c_{ij} - \frac{t_{ij}}{r_{ij}}) n_{ij\alpha} n_{ij\beta} + \frac{t_{ij}}{r_{ij}} \delta_{\alpha\beta}. \tag{4.9}$$

where t and c are the first and second derivatives of the bond energy with respect to bond length and $n_{ij\alpha}$ is the unit normal pointing from particle i to particle j. Then, $H_{i\alpha j\beta} = -M_{i\alpha j\beta}$ for off-diagonal terms and $H_{i\alpha j\beta} = \sum_j M_{i\alpha j\beta}$ for diagonal terms. However, for multibody potentials like the EAM potential the calculation of the Hessian matrix is more involved. For example, there can be non-zero terms in the Hessian matrix for a pair of particles i and j even when i and j are not the neighbors. Thus, the Hessian matrix for a multibody potential like EAM is less sparse than the one corresponding to a pair potential.

The particle velocities computed using this formulation are used in section 4.4.

4.2.2 3 D Simulation

We perform computational nano-indentation on a face-centered cubic (FCC) lattice using a spherical indenter of radius R. The indenter moves along the [1 0 0] direction to indent an L-J crystal. The load stepping algorithm is the same as in the two dimensional simulations, section 4.2.1. When nucleation occurs, we take an indenter step back, reduce the step size by a factor of 10 and restart our simulation. The load vs. depth curve for system size, $L = 65$ and indenter radius, $R = 25$ for fully 3D simulations is shown in Fig. 4.3. The analytic expression for load vs. indenter depth based on Hertzian contact theory for indentation by parabolic indenter on an anisotropic half space was given by Willis [41]. A spherical indenter can be approximated by a parabolic indenter up to first order. In general for an anisotropic half space the contact area is elliptical, however the 4-fold symmetry in the (100) plane results in circular contact area. In this case F vs. D is given by:

$$F = 4/3E^* R^{1/2} D^{3/2}. \tag{4.10}$$

E^* is the indentation modulus defined in [41]. As shown in Fig. 4.3, the analytical Hertzian model fits our simulation results up to the linear regime. The velocity field is computed using (4.8) as in 2D. However, diagonalization of a Hessian matrix for a fully three dimensional system can be computationally very expensive. The system considered for this work contains approximately 100,000 atoms. At the onset of instability in three dimensional simulations, there are two planes of atoms slipping with respect to each other resulting in nucleation of a dislocation loop. The critical

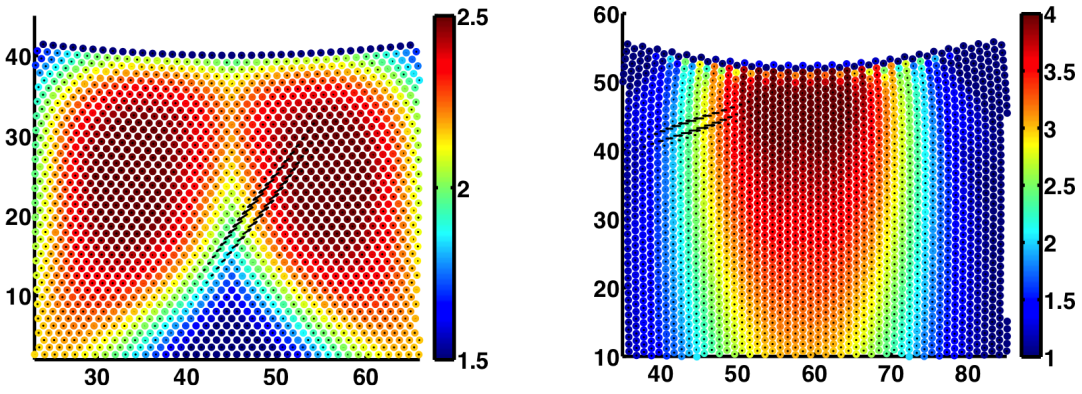

(a) (b)

Figure 4.4: The Schmid stress, τ for each atom in L-J crystal just before dislocation nucleation, O_1, $R = 120$ and O_2, $R = 50$. τ is not maximum at the point of instability. The arrows at each atom represent velocity field.

slip plane for an FCC lattice is one (111) plane and the slip direction is $< 1\bar{2}1 >$. Just before nucleation, the slipping plane or the embryo structure is shown in Fig. 4.12a where the colors represent the magnitude of the velocity field at each atom.

4.3 Analysis of Existing Criteria

4.3.1 The Schmid stress

The simplest attempt to predict the dislocation nucleation process in terms of a single material parameter involves computing appropriate projections of the atomic-level shear stress [42]. Within this framework, it is assumed that a dislocation loop will nucleate when the resolved shear stress, τ, on a given plane exceeds some threshold

value, τ_{crss}. This idea is similar to commonly known local yield stress criteria,

$$\tau \geq \tau_{crss} \tag{4.11}$$

where,

$$\tau = \max_{s,n} |s.T.n| \tag{4.12}$$

and T is the Cauchy stress tensor. At the embryo, s and n should predict the slip direction and the slip plane normal respectively. It is well established that the existing dislocations become mobile when the resolved shear stress, τ, on a dislocation reaches a critical value, τ_{crss}. This idea was extended to predict nucleation. In Fig. 4.4 the resolved shear stress, τ, just before instability is shown for two different crystal orientations of L-J crystal. The figure shows that τ is not maximum at the nucleation embryo core and hence, does not predict dislocation nucleation. In many previous studies [8] [22] [21], this idea that the Schmid stress controls dislocation nucleation has been shown to be incorrect.

4.3.2 Phonon Stability Criterion (Λ)

Li et al. [8] developed a criterion, called Λ criterion, based on Hill's [14] analysis of the stability of plane waves in a stressed, elastic continuum. Λ is related to the acoustic matrix A defined below which gives the vibrational frequencies of phonons of a given wavevector, k, and polarization direction, p. It is calculated for a homogeneously deformed crystal with deformation gradient equal to local atomic deformation gradient

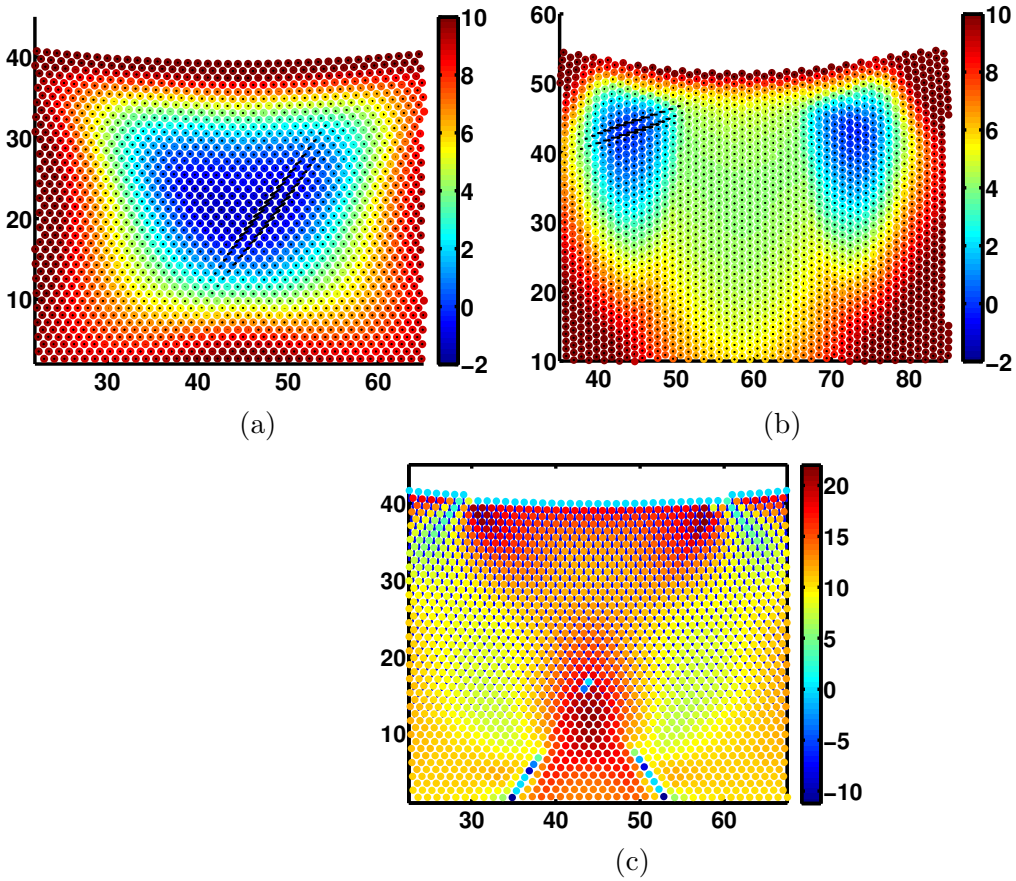

Figure 4.5: Phonon Stability Criterion, Λ value for each atom in L-J crystal (a) O_1, $R = 120$, just before nucleation (b)O_2, $R = 50$, just before nucleation (c)O_1, $R = 120$ after nucleation. Λ is negative in a large region around the dislocation core, so it is difficult to judge the precise location of the core. Moreover, Λ decreases further after nucleation when there is no real nucleation in the system.

at i^{th} particle:

$$A_{i\mu\nu}(\hat{k}) = \lim_{|k|\to 0} \frac{1}{|k|^2} D_{i\mu\nu}(k), \tag{4.13}$$

where $|k| := \sqrt{k_\alpha k_\alpha}$ is the magnitude of the wavevector k, $A_{i\mu\nu}$ is a 3×3 matrix indexed by μ, ν, defined at i^{th} particle and the dynamical matrix, $D_{i\mu\nu}$, in the long-wavelength approximation can be computed as

$$D_{i\mu\nu}(k) = |k|^2 \sum_j -0.5 H_{\mu\nu}(R_{ij\alpha})(\hat{k}_\beta R_{ij\beta})^2, \tag{4.14}$$

and $\hat{k}$ represents the unit vector corresponding to the wavevector k. $R_{ij\alpha}$ is the displacement vector defined from the i^{th} particle to the neighboring particle, j, in the homogeneously deformed crystal. $H_{\mu\nu}$ contains the elements of the Hessian matrix for a homogeneously deformed crystal.

Λ is defined as the minimum eigenvalue of the acoustic tensor A over all directions $\hat{k}$ on the unit sphere i.e.

$$\Lambda = \inf_{\hat{k}} \min_{\beta} \; eig_\beta \; A(\hat{k}), \tag{4.15}$$

where $eig_\beta \; A(\hat{k})$ represents the β^{th} eigenvalue of the matrix $A(\hat{k})$, and β takes values in the set $\{1, 2, 3\}$.

Λ corresponds to the least stable plane-wave perturbation, with $\Lambda = 0$ indicating an unstable mode. Alternatively, $\Lambda = 0$ may as well be interpreted as the criterion for loss of strong ellipticity of the governing equations of elasticity from a homogeneously deformed state. Thus, one seeks vectors (p, n) s.t. $[\mathscr{L}_{rmiq} p_r n_m p_i n_q] = 0$

with $\mathscr{L}$ defined in (4.22), and the energy function ψ defined as a function of the local atomic deformation gradient based on the Cauchy-Born hypothesis. Recently, MR [10] showed that Λ becomes negative before the actual instability and hence, loses the conceptual framework. The detailed calculation of Λ is shown in [36]. Λ for the L-J potential for the stable surface orientation O_1 and the unstable surface orientation O_2 is shown in Fig. 4.5. In all cases we observe that Λ is minimum at the embryo core. Note that Λ is also negative at the other symmetrically located embryo core. These results qualitatively remain the same for EAM Al potential as shown in [36]. However, as shown in Fig. 4.5c, Λ decreases further after nucleation around the dislocation cores, when there is no real nucleation in the system. Hence, this criterion cannot be used to predict the nucleation instant. Moreover, Λ is negative in a large region around the embryo core and is therefore complicated for identifying the exact location of the core.

4.3.3 Stress Gradient Criterion

The stress-gradient based criterion [5] identifies the embryo core through a quantity $N_{m,l}$ at each point in the crystal defined as

$$N_{m,l} = \max_{m,l} |m.curlT.l|, \tag{4.16}$$

where, m and l are unit vectors in the direction of Burgers vector and line direction respectively for the nucleating dislocation. T is the stress tensor. According to the criterion, if $N_{m,l}$ is greater than a critical value, N_{crit}, nucleation occurs. $N_{m,l}$ for

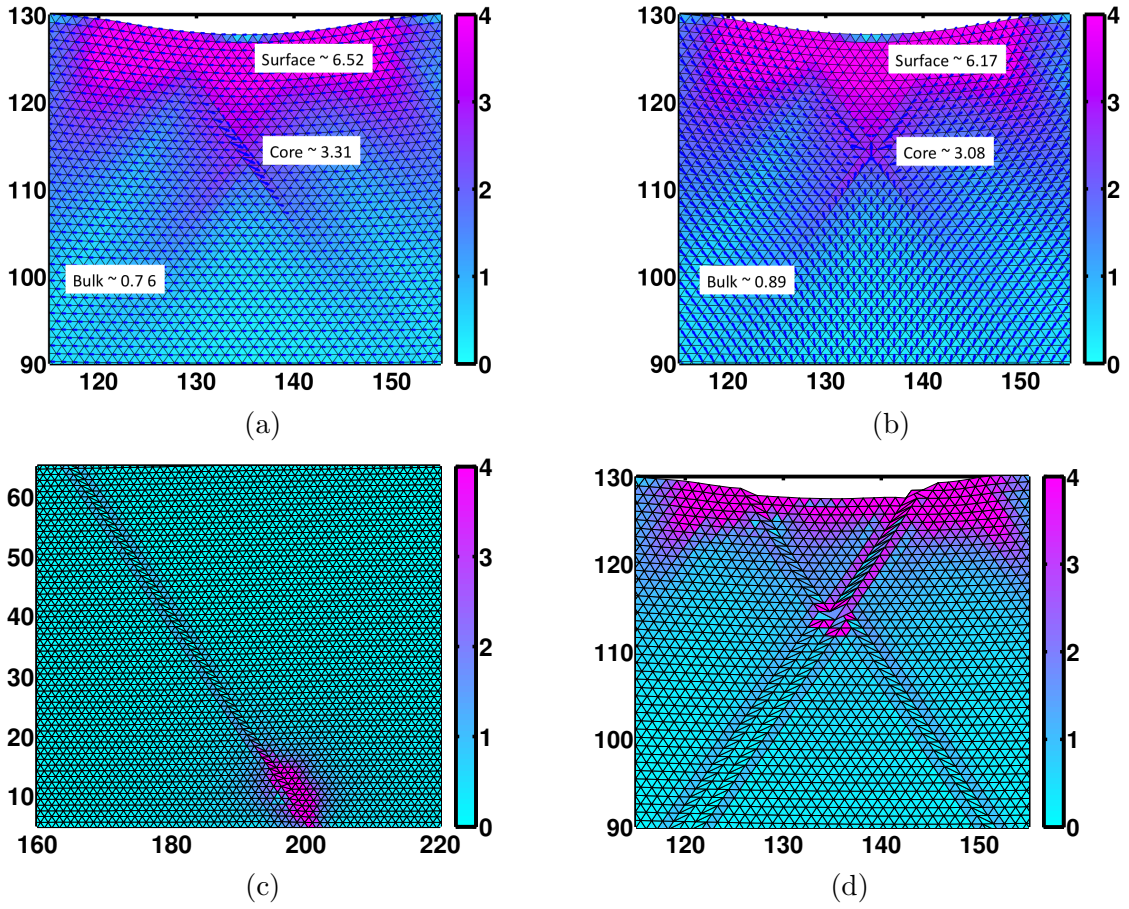

Figure 4.6: Stress Gradient Criterion, maximum $N_{m,l}$ value for each atom in L-J crystal, $R = 40$, in (a) non-symmetric configuration just before nucleation; (b) symmetric configuration, similar to MA [5] 2004, just before nucleation; (c) non-symmetric configuration, after nucleation; (d) symmetric configuration, after nucleation. Similar to Λ, $N_{m,l}$ increases further after nucleation when there is no real nucleation in the system. Also, $N_{m,l}$ is high near the surface so only the bulk has to be considered to calculate the precise location of nucleation, that makes the analysis complex.

two different indentation geometries in L-J crystal, O_1 is shown in Fig. 4.6a and 4.6b just before the nucleation. In Fig. 4.6b, the indenter is symmetrically located with respect to the crystal. This results in nucleation of two symmetrically located embryo loops. The geometry in Fig. 4.6b is similar to the system in [5], however the interatomic-potential and indenter radius are different. Our results are qualitatively similar to [5], with $N_{m,l}$ high at the core along with the surface. However, the thickness of the high $N_{m,l}$ region at the surface is greater than in [5].

We observed that $N_{m,l}$ is highest at the embryo core in the bulk for all the systems considered. However, similar to Λ, $N_{m,l}$ fails to predict the nucleation instant. It increases further near the dislocation cores after nucleation, when there is no actual nucleation in the system. This observation for Λ and $N_{m,l}$ was also made by MR [10].

4.4 Linear Stability of Dislocation Density Evolution in Field Dislocation Mechanics

4.4.1 Formulation of Criterion

We perform linear stability analysis of the equation for evolution of the dislocation density field in finite deformation Field Dislocation Mechanics (FDM). We begin

with the evolution equation written in Eulerian form [38]:

$$\frac{\partial \alpha}{\partial t} = -curl(\alpha \times (v + V)) + s, \tag{4.17}$$

where the time derivative corresponds to the spatial representation of the α field. Here, α is the dislocation density tensor, v is the material velocity vector, V is the dislocation velocity vector *relative to the material* and s is a dislocation nucleation rate tensor. A requirement is that s be the *curl* of a tensor field. The statement (4.17) arises as the local form of an areal balance statement for Burgers vector content:

$$\frac{d}{dt}\int_{p(t)} \alpha\, n\; da = \int_{c(t)} \alpha \times V dx + \int_{a(t} s\, n\; da, \tag{4.18}$$

where $p(t)$ is any oriented area patch of material particles (with unit normal field n) convecting with the material velocity and $c(t)$ is its closed boundary curve.

With $s = 0$, (4.17) may also be viewed as a statement of conservation of $\int_B \alpha\; dv$ for any fixed spatial volume B in the absence of any flux of α carried into B by the velocity field $v + V$. However, since α is a 'signed' density, unlike conservation statements for strictly positive scalar density fields like mass, this conservation statement allows nucleation of dislocation density fields within B whose volume integral vanishes, e.g. a single loop contained within B. In the spirit of doing more with less, we therefore utilize (4.17) with $s = 0$. Our strategy in this paper involves supplying (4.17) with a finite-element interpolated (quasi-static) material velocity field from atomistic simulations in which nucleation is monitored, and probing linear stability of perturbations to the α field in (4.17). In addition, our primary interest here is

simply in homogeneous nucleation, so we linearize (4.17) about the state $\alpha = 0$. For any physically reasonable constitutive equation for the dislocation velocity V, it may be assumed that $V = 0$ if $\alpha = 0$.

Then,

$$\frac{\partial \delta\alpha}{\partial t} = -curl((\delta\alpha \times (v + V)) + (\alpha \times \delta v) + (\alpha \times \delta V)), \tag{4.19}$$

and since $V = 0$ here, the governing equation for linear stability analysis becomes

$$\frac{\partial \delta\alpha}{\partial t} = -curl(\delta\alpha \times v). \tag{4.20}$$

In terms of components with respect to a rectangular Cartesian coordinate system, (4.20) can be written as

$$\frac{\partial \delta\alpha_{ij}}{\partial t} = -e_{jrs}(\delta\alpha_{im} v_n e_{smn})_{,r} \tag{4.21}$$

where e_{jrs} is a component of the third-order alternating tensor.

As mentioned before, in our analysis to follow, we utilize a material velocity field obtained from atomistic simulations. For the sake of completeness, we list here the continuum governing equation controlling that velocity field in the special case of an elastic material before any nucleation has happened (including the state for incipient nucleation). Quasi-static balance of linear momentum is the statement

$$div[T] = 0 \tag{4.22}$$

where, T is the Cauchy stress tensor and the div operator is on the current configuration. Converted to the statement of continuing equilibrium (or the 'rate form') we obtain

$$div\left[div(v)T + \dot{T} - TL^T\right] = 0,$$

and for an elastic material with a free-energy density per unit mass given by $\psi(F)$, where F is the deformation gradient from the stress-free elastic reference, continuing equilibrium can be further written as

$$div[\mathscr{L}L] = 0, \tag{4.23}$$

where, $\mathscr{L}_{rmiq} = \rho F^T_{sm}\frac{\partial^2\psi}{\partial F_{rs}\partial F_{ij}}F^T_{jq}$ is the fourth order tensor of incremental moduli, ρ is the mass density, and L is the velocity gradient. Of course, these equations apply to the atomistic material only under the *strong* assumption that $\psi(F)$ is an adequate representation of the energy density of the crystal.

Henceforth, we use the notation $\delta\alpha = a$. (4.21) can be rewritten as

$$\frac{\partial a_{ij}}{\partial t} + a_{ij,r}v_r = v_{j,m}a_{im} - v_{r,r}a_{ij}. \tag{4.24}$$

In terms of the material time derivative, (4.24) is equivalent to

$$\begin{aligned} \frac{da_{ij}}{dt} &= K_{ijrm}a_{rm} \\ K_{ijrm} &= \left(v_{j,m}\delta_{ir} - v_{k,k}\delta_{ir}\delta_{jm}\right), \end{aligned} \tag{4.25}$$

and (4.25) constitutes the governing equation for the perturbation field a of the dislocation density. It is to be noted that (4.25) represents the vanishing of the (back-leg) contravariant convected derivative [43] of the two-point tensor a with respect to the time-dependent tensor function $\frac{1}{J}F$ with $J = detF$ and F being measured from an arbitrarily fixed reference configuration:

$$tr(L)a + \frac{da}{dt} - aL^T = \frac{d\left(aJF^{-T}\right)}{dt}\frac{1}{J}F^T = 0. \tag{4.26}$$

With the material velocity considered as a given field, this is simply the linearization of the statement that the convected derivative of the two-point tensor field α vanishes, i.e.

$$div(v)\alpha + \frac{d\alpha}{dt} - \alpha L^T = 0. \tag{4.27}$$

This is the Lagrangian equivalent of (4.17) under the assumption that $V = 0$, $s = 0$ and $div\ \alpha = 0$ [38], stating that the Burgers vector content of a material area patch remains constant in the absence of dislocation sources and if the existing dislocations threading the patch do not move with respect to the material.

We note that with the velocity gradient field considered as a given input, (4.25) constitutes a pointwise system of ordinary differential equations (ODE) for the perturbation array a. For approximate analysis of stability of this system, we consider it as a constant coefficient system of ODE governed by the velocity gradient field at every point. For the analysis of growth of perturbations it helps to consider the components of a_{ij} as a 9×1 vector A and $(v_{j,m}\delta_{ir} - v_{k,k}\delta_{ir}\delta_{jm})$ as a 9×9 array

denoted by $\mathscr{N}$ to write (4.25) as

$$\frac{dA}{dt} = \mathscr{N} A. \tag{4.28}$$

If at any stage of deformation an eigenvalue of $\mathscr{N}$ has a positive real part at any point of the body, then that state is deemed to be 'linearly unstable' and susceptible to the nucleation of a dislocation. Of course, linear stability is only conclusive with respect to stability, so for conditions of instability, we treat such positivity as a necessary condition and probe magnitudes of the real parts of the eigenvalues as well.

We denote the maximum of the real parts of the eigenvalues of $\mathscr{N}$ at any point by the value of the field η at that point.

To understand growth of the dislocation density field at the instant of incipient instability, we note that (4.25) implies

$$\frac{d\,(a_{ij}a_{ij})}{dt} = 2a_{ij}(D_{jm}\delta_{ir} - D_{kk}\delta_{ir}\delta_{jm})a_{rm}, \tag{4.29}$$

where D is the symmetric part of the velocity gradient L, and we observe that our nucleation criterion has the correct limiting behavior in the case of rigid motions, implying that no growth of perturbations in dislocation density (i.e. nucleation) is possible from a dislocation-free state in the case of arbitrary rigid motions. More interestingly, we note the following facts.

4.4.2 Convected rate vs. Jaumann rate

While in our theory the convected derivative with respect to $\left(\frac{1}{J}F\right)$ appearing in (4.27) is a non-negotiable ingredient implied by the necessity of doing calculus on a body occupying coherent regions of space parametrized by time, considerations of frame-indifference alone would allow the convected rate to be posed as any appropriate objective rate for the two-point tensor field α. In particular, if one were to arbitrarily choose the analog of the Jaumann rate for this two-point tensor field, i.e. the convected rate with respect to the orthogonal tensor R^* that at each point of the body satisfies $\frac{dR^*}{dt} = \Omega^* R^*$, where Ω^* is the material spin (the skew-symmetric part of the velocity gradient L), then (4.25), (4.27), and (4.29) imply that nucleation would never be possible.

4.4.3 Volterra and Somigliana distributions

Further insight into the possible predictions of nucleation from (4.25) can be obtained by considering velocity fields with 'planar' spatial variation in only the x_1 and x_2 directions and dislocation density perturbations to be constrained to only $a_{i3} \neq 0$ (i.e. straight dislocations with x_3 as line direction). Then (4.24) directly implies

$$\frac{da_{i3}}{dt} = -v_{r,r}a_{i3}. \tag{4.30}$$

In particular, planar simple shearing in the x_1 direction (only the v_1 component as non-zero) on planes normal to x_2 with variation only in the x_2 direction can cause no

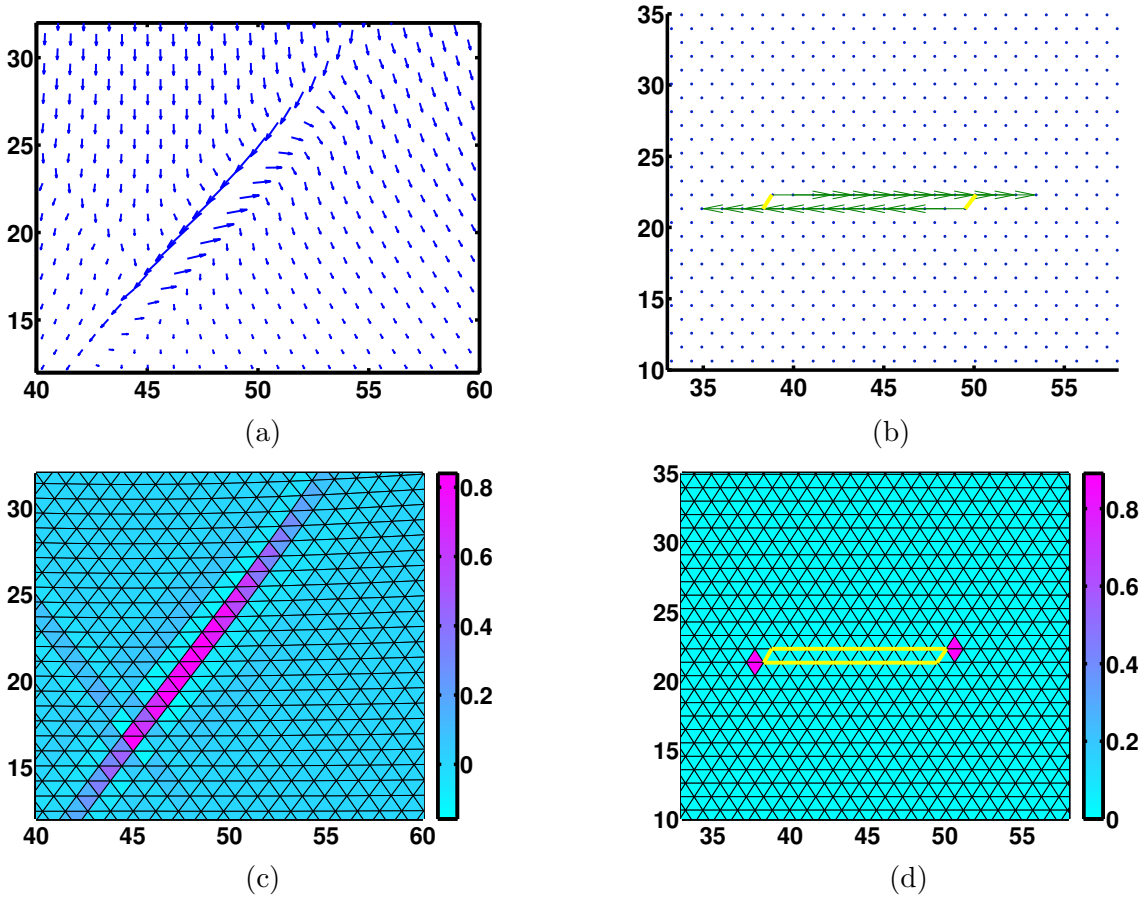

Figure 4.7: L-J crystal, O_1 (a) Velocity field for R = 120, just before nucleation. (b) Idealized velocity field for nucleation of a Volterra dislocation dipole. (c) η calculated using linear stability of FDM, for velocity field in (a). (d) η, for velocity field in (b); The yellow-lines in (b) and (d) show the position of the slip embryo. Because of the continuously distributed slip distribution as shown in case (a) η is non-local as shown in (c). On the other hand, in (d) η is localized at the points of nucleation because of sharp drop-offs in slip at the boundary of embryo in (b).

nucleation of straight dislocations threading the $x_1 - x_2$ plane (assuming these are the only type of dislocations that are allowed). However, if there exists a slip-direction gradient of the shear strain-rate field, i.e. $v_{1,21}$ is non-zero, then the compatibility of the velocity gradient field (equality of the second partial derivatives) implies that $v_{1,1}$ must be non-zero at such points and that this can cause nucleation of straight edge dislocations according to our criterion (and similarly for the nucleation of straight screws corresponding to shearing in the x_3 direction with in-plane spatial variations). In particular, if we have an incipient slip embryo where the v_1 component is uniform in the x_1 direction except for sharp drop-offs at the boundary of the embryo, then the possibility of a nucleating a Volterra edge dipole exists as shown in Fig. 4.7b and 4.7d. On the other hand, if the v_1 field varies smoothly along the x_1 direction within the embryo then the possibility nucleating a true continuously distributed dislocation density field exists, corresponding to a Somigliana distribution, as shown in Fig. 4.7a and 4.7c. In the simulations of section 4.4, a Somigliana distribution is what appears to nucleate in atomic configurations under load.

Equation (4.30) was based on the assumption that only $a_{i3} \neq 0$; however, we note here that Figs. 4.7c and 4.7d are plots of the η field from calculations that allows for all possible dislocation density perturbations, using the driving velocity fields shown in Figs. 4.7a and 4.7b, respectively. In section 4.5, results utilizing actual atomistic, nanoindentation velocity fields are reported.

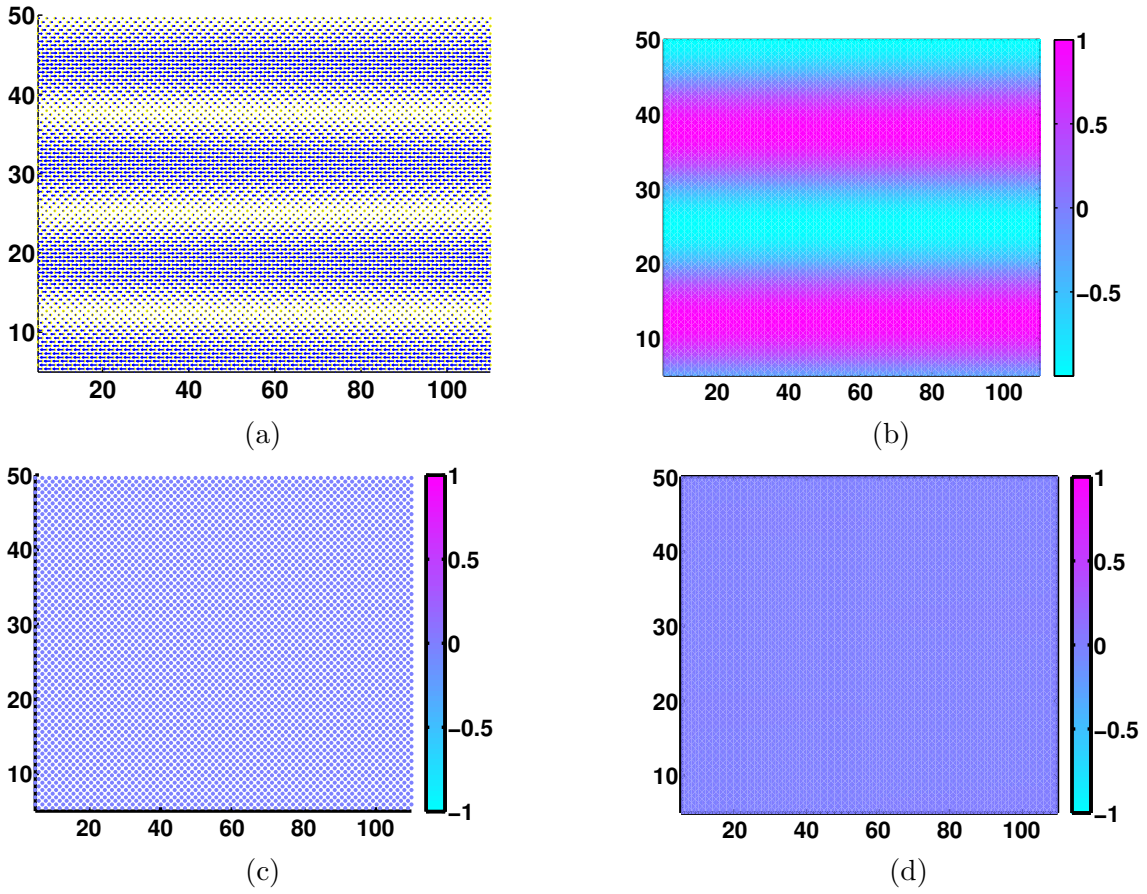

Figure 4.8: L-J crystal, O_2 (a) Critical eigenmode for homogeneous compression just before bifurcation. (b) Ω/Ω_{max} corresponding to the mode. (c) Λ, Λ decreases by an order of magnitude and is almost zero in the whole configuration just before bifurcation. (d) η, η is almost zero everywhere and does not show dislocation nucleation.

4.4.4 Shear band/phase boundary and dislocation nucleation

The nucleation of an ideal shear band or a pair of phase boundaries without terminations within the body are cases that are controlled by the occurrence of localized transverse gradients of the velocity field with respect to some planes. Here, by a phase boundary we mean a single surface in the body across which the deformation gradient is discontinuous; by a shear band we mean two such surfaces separated by a small distance, and ânon-terminatingâ refers to the fact that these discontinuity surfaces run from one external surface of the body to another. Maloney et al. [36] defined Ω as the transverse derivative of the velocity field with respect to the slip direction to identify location of dislocation nucleation. The Ω field in Fig. 4.8b is high for the long-wavelength mode shown in Fig. 4.8a, that is not a case of nucleation of dislocation dipole. Fig. 4.8a shows a smooth buckling mode from a state of homogeneous compression. The mode is the linearized precursor of a long-wavelength nonlinear instability that occurs in this simulation with a flat indenter. Note that in the case of homogeneous compression the critical mode is completely non-local and extends to full system size, as compared to the critical mode for nano-indentation discussed in section 4.2.1. In this case of the long-wavelength instability, η is close to 0 and does not predict dislocation nucleation as shown in Fig. 4.8d. In the case of a simple shear where $v_{1,2}$ is non-zero and $v_{1,1}$ is zero, η would be zero, whereas Ω would be high.

For this case of homogeneous compression, Λ is almost 0 in the entire configuration as shown in Fig. 4.8c. Since Λ is 0, it is reasonable to check whether a localized velocity

mode with polarization and plane normal predicted using Λ is also an eigenmode of the discrete atomistic Hessian matrix, as a check of the adequacy of local continuum elastic response in reflecting the elasticity and instabilities of the atomic lattice. As alluded to in the previous paragraph, we verified that a localized shear band mode predicted by the continuum analysis is *not* an eigenmode of the atomistic stiffness matrix even though Λ is 0. This difference can be attributed to the atomistic details in the stiffness or the Hessian matrix; roughly speaking, an atomistic model may be assumed to correspond to higher than second-order boundary value problems and the linearization of such a system governing instabilities is naturally different from that of the corresponding second-order system. This analysis suggests that Λ cannot always be used even for the case of phase boundary nucleation. Moreover, in this case of homogeneous compression, Λ is critical i.e. 0 everywhere and its critical eigenmode does not correspond to the nucleation of a dislocation dipole.

4.4.5 Hydrostatic Compression

In the fully 3-D simulations if a pure hydrostatic velocity field is considered, then

$$v_{j,m} = e\delta_{jm} \tag{4.31}$$

where, e is a constant and (4.25) becomes

$$\frac{da_{ij}}{dt} = -2ea_{ij}. \tag{4.32}$$

Since e is negative for compression, a_{ij} always shows growth. As shown in section 4.5, our analysis requires η should grow by orders of magnitude for implying dislocation nucleation. In this case of hydrostatic compression, if the compression rate is uniform then η would be constant and would not indicate nucleation. However, by the same token, were a non-uniform-in-time, purely hydrostatic compression state to be achieved in a real deformation, then the FDM based indicator would imply growth of dislocation density.

Leaving aside the question of the physical merit of this case, the reason behind this awkward implication may be understood as follows. From a dislocation-free state, a governing constraint behind the prediction of growth of dislocation perturbations is (4.27) which is equivalent to

$$\frac{d}{dt}\int_{p(t)} \alpha n \, da = 0$$

for any material area patch $p(t)$ in the body, and the net Burgers vector of any area patch is conserved. Thus, if a deformation tends to shrink areas then the dislocation density has to grow to conserve the Burgers vector content of the perturbation. Interestingly, it appears that it is this kinematic 'mechanism' that predicts correct trends for the initiation of dislocation nucleation as shown in the results of this paper. Of course, once the dislocation density perturbation grows, subsequent states of evolution have non-zero dislocation density and then Burgers vector content of area patches is also affected by the flow term $\alpha \times V$ and its spatial variation.

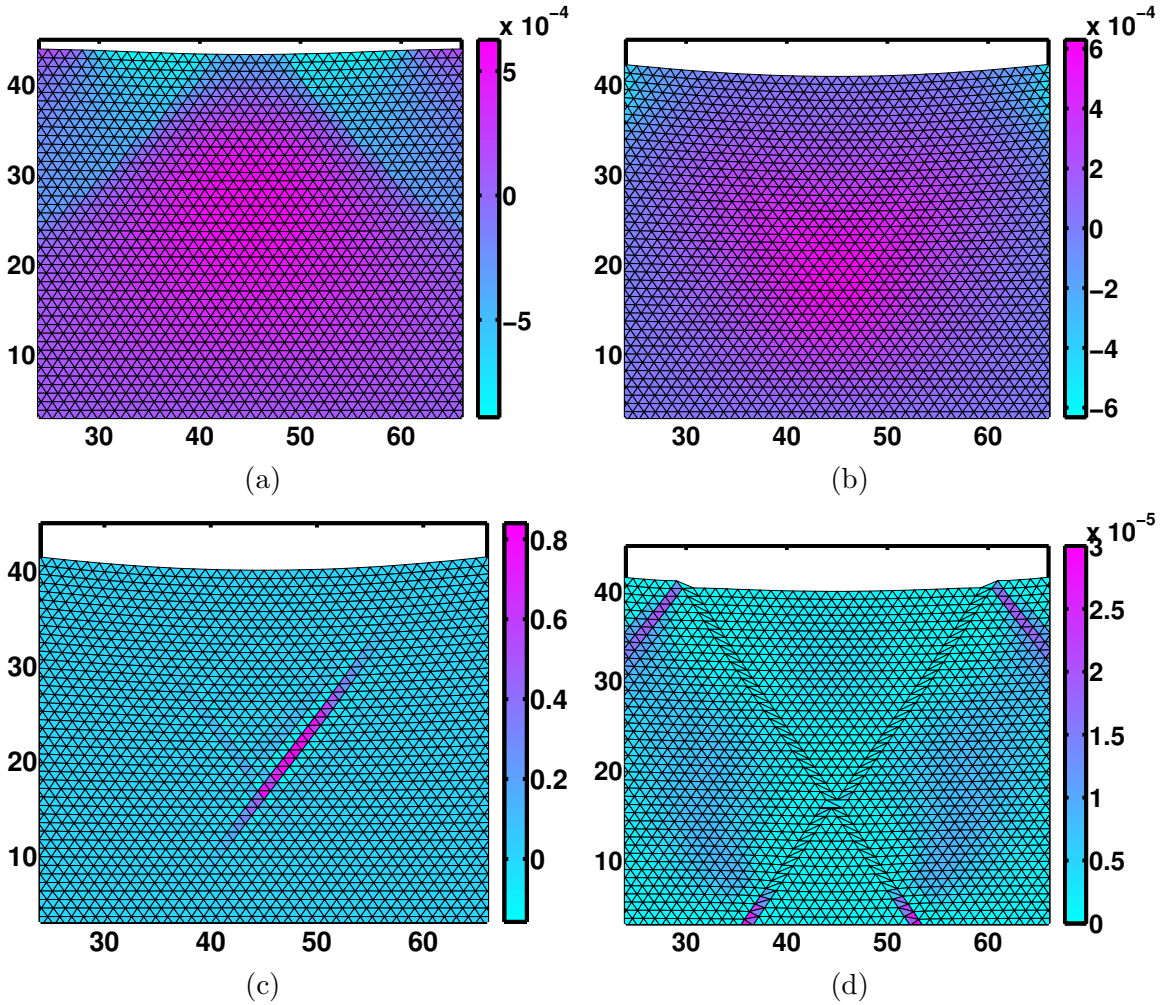

Figure 4.9: η calculated using linear stability of FDM for L-J crystal, O_1, $R = 120$ in (a),(b) much before dislocation nucleation event; (c) just before nucleation; (d) after nucleation. η is precisely maximum at the embryo. It decreases by order of magnitudes after nucleation.

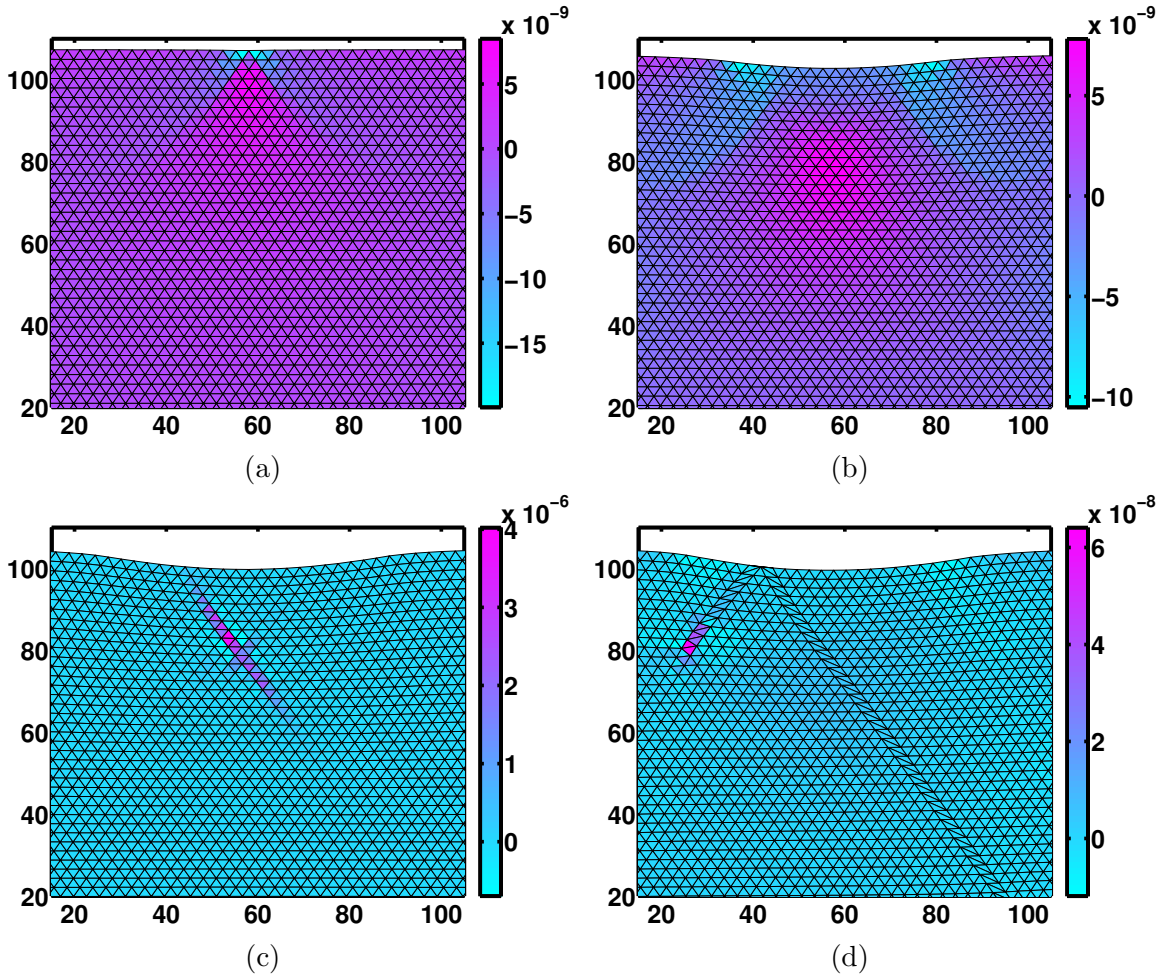

Figure 4.10: η calculated using linear stability of FDM for EAM-Al. crystal, O_1, $R = 40$ in (a),(b) much before dislocation nucleation event; (c) just before nucleation; (d) after nucleation. η is precisely maximum at the embryo. It decreases by order of magnitudes after nucleation.

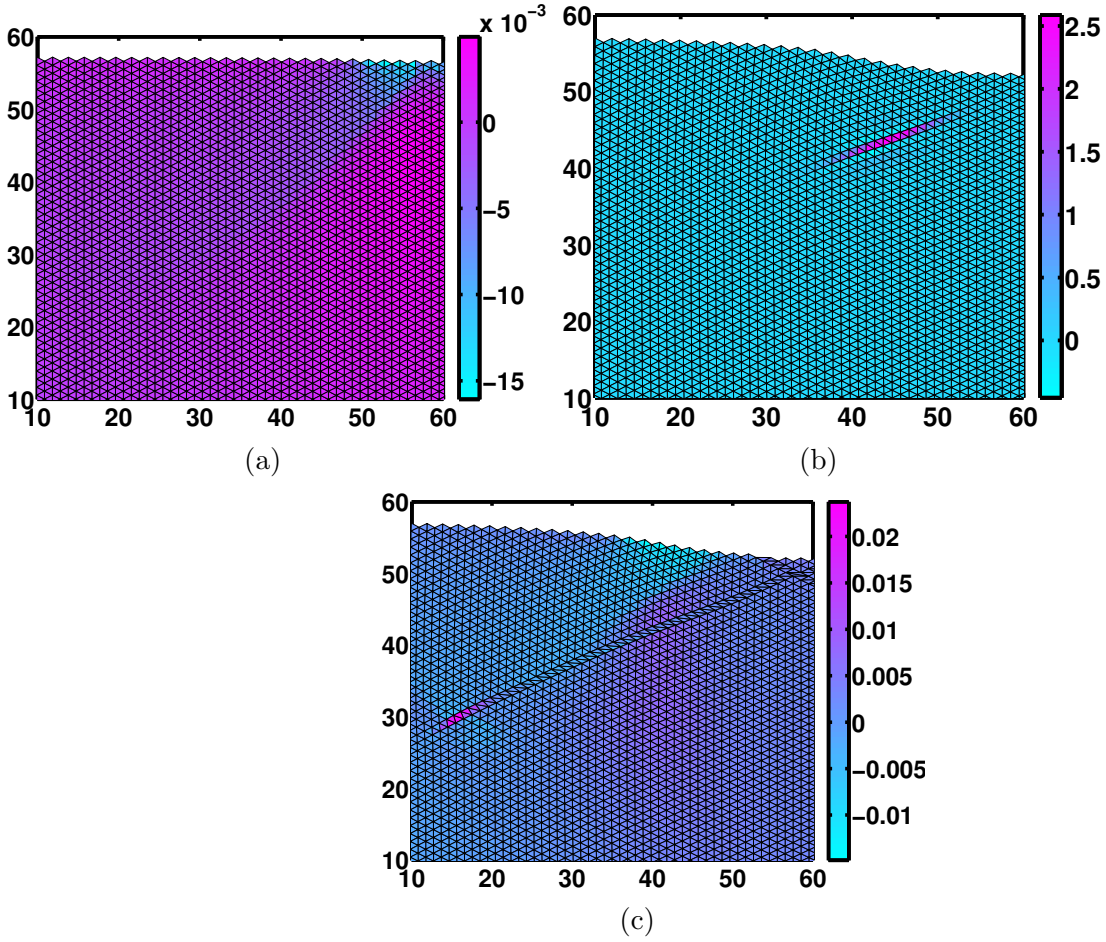

(a) (b)

(c)

Figure 4.11: η calculated using linear stability of FDM, for L-J crystal, O_2, $R = 50$ in (a) much before dislocation nucleation event; (b) just before nucleation; (c) after nucleation. η is precisely maximum at the embryo. It decreases by order of magnitudes after nucleation. Only one-half of the crystal in which dislocation nucleation happens is shown.

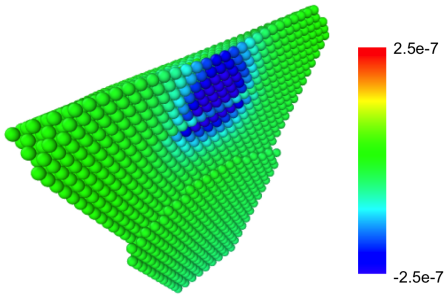

(a)

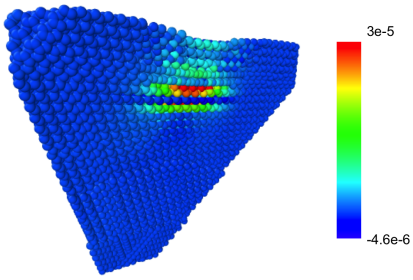

(b)

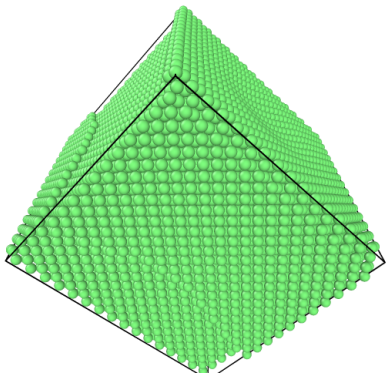

(c)

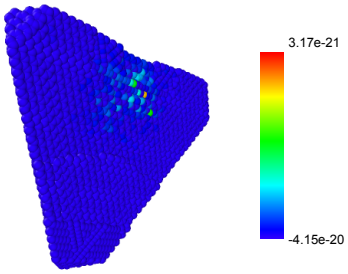

(d)

Figure 4.12: L-J 3D - FCC crystal, $R = 25$. Indentation axis is along [1 0 0] axis. The crystal is sliced along the plane (111). The colors represent: (a) Velocity field magnitude; (b) η, note that the balls plotted in this figure are located at the centroid of tetrahedrons formed by atoms where η is calculated. Similar to 2D, in fully 3D simulations η increases by two orders of magnitude just before nucleation and it decreases by two orders of magnitude after nucleation. The full FCC Lattice is shown in (c). There are periodic boundaries conditions in the normal directions to the indentation axis. Black solid lines in (c) show the periodic box size. (d) η computed by substituting the Convected rate by Jaumann rates in the linear stability analysis of FDM. Interestingly only the emergent convected rates from linear stability analysis show instability.

4.5 Results

We mesh both two and three dimensional systems using Delaunay triangulation. Using section 4.2.1, particle velocities are known at each atom or node. We use linear shape functions to interpolate these velocities on each element and compute derivatives. The velocity derivatives are needed to calculate the maximum positive real part of eigenvalues of $\mathscr{N}$, η, at the centroid of each triangle (in 2D) or tetrahedron (in 3D). In all figures in this work, the arrows correspond to the particle velocity. In two dimensional simulations, there are two planes of atoms slipping against each other as shown in Fig. 4.4 and give rise to a pair of dislocations.

For orientation O_1, the spatial η field is shown at various indenter depths for L-J crystal in Fig. 4.9. η is around 6×10^{-4} much before nucleation as shown in Figs. 4.9a and 4.9b. Note that positive η does not necessarily imply nucleation, this being a limitation of constant-coefficient linear stability analysis. Just before nucleation, η increases by three orders of magnitude. Also, it is highly positive only for the triangles formed by atoms on the slipping planes. After nucleation, η decreases by four orders of magnitude and does not persist at the dislocation cores. In Fig. 4.10, we show similar analysis for EAM-Al crystals. Initially η is around 6×10^{-9} and just before nucleation it increases by three orders of magnitude. Similar to L-J, for the EAM-Al crystal, η drops by three orders of magnitude after nucleation. Similar results are observed for L-J O_2 orientation in Fig. 4.11. Even though before nucleation η depends on the crystal orientation and inter-atomic potential, it increases by three orders of magnitude just before nucleation and decreases by the same amount after

nucleation for all systems in 2D.

In Fig. 4.12a, 4.12b and 4.12d, results for the fully 3D simulations are shown. In these figures the FCC lattice is sliced along the plane containing the unstable embryo. In Fig. 4.12a the colors represent the magnitude of velocity field. Long before nucleation, η is around 3×10^{-7}. Just before nucleation, η increases by two order of magnitude as shown in Fig. 4.12b and then, after nucleation it drops by roughly two orders of magnitude as in Fig. 4.12d.

For predicting the line direction, l, we calculated the eigenmodes of $\mathscr{N}$. The eigenmodes correpond to the nucleating dislocation density tensor. At the points of interest, $\mathscr{N}$ had more than one eigenvalues with positive real part. We verified that the nucleating dislocation density tensor lies in the linear span of the eigenmodes of the eigenvalues with positive real parts. An expression for predicting the line direction, l, was formulated in [40] as shown in (4.33). This expression is related to the stress gradient criterion described in section 4.3 and is given by

$$l = grad\tau \times n. \tag{4.33}$$

τ is the resolved shear stress on the slip plane with normal n. We find that (4.33) predicts the line direction correctly only for edge dislocations, where the line direction is normal to the Burgers vector. For mixed dislocations, the stress gradient criterion predicts only the edge component of the actual line direction.

In (4.24) the convected rate emerges naturally. If we replace the convected rate by the analog of the Jaumann rate for a two-point tensor, $\mathscr{N}$ becomes a skew-symmetric

matrix. A skew-symmetric matrix always has imaginary eigenvalues and can never be positive-definite. Hence, the Jaumann rate based $\mathscr{N}$ cannot predict nucleation. The numerical result for maximum eigenvalue of the Jaumann rate based $\mathscr{N}$, just before nucleation, is also shown in Fig. 4.12d. As the discussion surrounding (4.29) shows, it does not predict nucleation.

4.6 Concluding Remarks

The kinematics of dislocation density evolution in FDM appears to be sufficiently versatile in embodying homogeneous dislocation nucleation within the theory and for developing criteria that can be used in other modeling paradigms. In order to isolate and understand this capability, we have tested the feature with atomistically generated velocity fields that, obviously, have analogs in coarser-than-atomic-scale simulation models like Discrete Dislocation Dynamics and Field Dislocation Mechanics. In this sense, our analysis represents an advance in putting forward a conceptual framework for dislocation nucleation that naturally connects to coarser scale models. A main question that arises at this point is the extent to which these coarser length scale models can produce the requisite material velocity fields. Clearly, nonlinear kinematics is important and our analysis in section 4.4.4 shows that dislocation nucleation criteria and associated velocity modes based on classical ideas of loss of strong ellipticity of nonlinear elastic models, even when driven by atomistic input through the Cauchy-Born (CB) hypothesis, may not always be adequate. However, during nano-indentation simulations that induce a strong inhomogeneous deforma-

tion, sufficiently close to the bifurcation point of the lattice statics calculation, the polarization direction and discontinuity-plane normal predicted from the (continuum) acoustic tensor corresponding to Λ predicts the correct slip plane and Burgers vector direction for the nucleating dislocation dipole. This holds irrespective of the crystallographic orientation and inter-atomic potential. Based on this evidence, dislocation nucleation criteria relying on velocity fields generated from CB-based continuum elasticity *coupled* with the FDM-based dislocation nucleation indicator we have developed herein appears to be a logical step to pursue in future work. Furthermore, higher-order elasticity can be folded into a framework like Field Dislocation Mechanics and even without resorting to nonlocal/gradient elasticity, FDM in the finite deformation setting incorporating a dislocation density contributing to core energy has a significantly different stress response function [39] than the classical case. The effect of such enhancements in predicted velocity fields from full nonlinear analyses remain to be explored.

Bibliography

[1] C. L. Kelchner, S. J. Plimpton, and J. C. Hamilton, "Dislocation nucleation and defect structure during surface indentation," *Physical Review B*, vol. 58, pp. 11085–11088, Nov. 1998.

[2] A. Gouldstone, K. J. Van Vliet, and S. Suresh, "Nanoindentation: Simulation of defect nucleation in a crystal," *Nature*, vol. 411, pp. 656–656, June 2001.

[3] O. Rodriguez de la Fuente, J. A. Zimmerman, M. A. Gonzalez, J. de la Figuera, J. C. Hamilton, W. W. Pai, and J. M. Rojo, "Dislocation emission around nanoindentations on a (001) fcc metal surface studied by scanning tunneling microscopy and atomistic simulations," *Physical Review Letters*, vol. 88, p. 036101, Jan. 2002.

[4] P. Meijers, "The contact problem of a rigid cylinder on an elastic layer," *Applied Scientific Research*, vol. 18, pp. 353–383, Jan. 1968.

[5] R. E. Miller and A. Acharya, "A stress-gradient based criterion for dislocation nucleation in crystals," *Journal of the Mechanics and Physics of Solids*, vol. 52, p. 1507â1525, 2004.

[6] G.I.Taylor, "The mechanism of plastic deformation in crystals," *Proceedings of the royal society*, 1934.

[7] R.Philips, "Crystals, defects, and micrstructures.," *Cambridge*, 2001.

[8] J. Li, K. J. Van Vliet, T. Zhu, S. Yip, and S. Suresh, "Atomistic mechanisms governing elastic limit and incipient plasticity in crystals," *Nature*, vol. 418, pp. 307–310, July 2002.

[9] K. Van Vliet, J. Li, T. Zhu, S. Yip, and S. Suresh, "Quantifying the early stages of plasticity through nanoscale experiments and simulations," *Physical Review B*, vol. 67, Mar. 2003.

[10] R. Miller and D. Rodney, "On the nonlocal nature of dislocation nucleation during nanoindentation," *Journal of the Mechanics and Physics of Solids*, vol. 56, pp. 1203–1223, Apr. 2008.

[11] L. M. Hale, X. Zhou, J. Zimmerman, N. Moody, B. R., and W. Gerberich, "Phase transformations, dislocations and hardening in uniaxially compressed silicon nanospheres," *Computational Matreial Science*, 2011.

[12] A. T. Jennings, C. R. Weinberger, S.-W. Lee, Z. H. Aitken, L. Meza, and J. R. Greer, "Modeling dislocation nucleation strengths in pristine metallic nanowires under experimental conditions," *Acta Materialia*, 2013.

[13] T. Zhu, J. Li, K. J. Van Vliet, S. Ogata, S. Yip, and S. Suresh, "Predictive modeling of nanoindentation-induced homogeneous dislocation nucleation in cop-

per," *Journal of the Mechanics and Physics of Solids*, vol. 52, pp. 691–724, Mar. 2004.

[14] R. Hill, "Acceleration waves in solids," *Journal of the Mechanics and Physics of Solids*, vol. 10, pp. 1–16, Jan. 1962.

[15] T. Zhu, J. Li, and S. Yip, "Atomistic study of dislocation loop emission from a crack tip," *Physical Review Letters*, vol. 93, July 2004.

[16] S. Plimpton, "Fast parallel algorithms for short-range molecular dynamics," *Journal of Computational Physics*, vol. 117, pp. 1–19, Mar. 1995.

[17] E. Jones, T. Oliphant, P. Peterson, *et al.*, "SciPy: Open source scientific tools for Python," 2001–. [Online; accessed 2014-08-28].

[18] F. Ercolessi and J. B. Adams, "Interatomic potentials from first-principles calculations," *MRS Online Proceedings Library*, vol. 291, pp. null–null, 1992.

[19] A. Hasan, "Saddle node scaling on approach to dislocation nucleation," *International Journal for Multiscale Computational Engineering*, 2011.

[20] A. Lemaitre and C. Maloney, "Sum rules for the quasi-static and visco-elastic response of disordered solids at zero temperature," *Journal of Statistical Physics*, vol. 123, pp. 415–453, Apr. 2006.

[21] J. Zimmerman, C. Kelchner, P. Klein, J. Hamilton, and S. Foiles, "Surface step effects on nanoindentation," *Physical Review Letters*, vol. 87, Oct. 2001.

[22] J. Li, T. Zhu, S. Yip, K. J. Van Vliet, and S. Suresh, "Elastic criterion for dislocation nucleation," *Materials Science and Engineering: A*, vol. 365, pp. 25–30, Jan. 2004.

[23] M. L. Falk and J. S. Langer, "Dynamics of viscoplastic deformation in amorphous solids," *Physical Review E*, vol. 57, pp. 7192–7205, June 1998. arXiv:cond-mat/9712114.

[24] T. Delph, J. Zimmerman, J. Rickman, and J. Kunz, "A local instability criterion for solid-state defects," *Journal of the Mechanics and Physics of Solids*, vol. 57, pp. 67–75, Jan. 2009.

[25] T. J. Delph and J. A. Zimmerman, "Prediction of instabilities at the atomic scale," *Modelling and Simulation in Materials Science and Engineering*, vol. 18, p. 045008, June 2010.

[26] C. Maloney and A. Lemaitre, "Amorphous systems in athermal, quasistatic shear," *Physical Review E*, vol. 74, July 2006.

[27] A. Acharya, "A model of crystal plasticity based on the theory of continuously distributed dislocations," *Journal of the Mechanics and Physics of Solids*, vol. 49, no. 4, p. 761â784, 2001.

[28] A. Acharya, "New inroads in an old subject: Plasticity, from around the atomic to the macroscopic scale," *Journal of the Mechanics and Physics of Solids*, vol. 58, no. 5, p. 766â778, 2010.

[29] W. W. Gerberich, J. C. Nelson, E. T. Lilleodden, P. Anderson, and J. T. Wyrobek, "Indentation induced dislocation nucleation: The initial yield point," *Acta Materiala*, vol. 44, p. 3585â3598, Sept. 1996.

[30] C. A. Schuh, J. K. Mason, and A. C. Lund, "Quantitative insight into dislocation nucleation from high-temperature nanoindentation experiments," *Nature Materials*, vol. 4, p. 617â621, Aug. 2005.

[31] J. R. Rice and G. E. Beltz, "The activation energy for dislocation nucleation at a crack," *Journal of the Mechanics and Physics of Solids*, vol. 42, pp. 333–360, Feb. 1994.

[32] J. R. Rice, "Dislocation nucleation from a crack tip: An analysis based on the peierls concept," *Journal of the Mechanics and Physics of Solids*, vol. 40, pp. 239–271, Jan. 1992.

[33] R. Peierls, "The size of a dislocation," *Proceedings of the Physical Society*, vol. 52, no. 34, 1940.

[34] F. R. N. Nabarro, "Dislocations in a simple cubic lattice," *Proceedings of the Physical Society of London*, vol. 59, no. 332, p. 256â272, 1947.

[35] V. Vitek, "Intrinsic stacking faults in body-centered cubic crystal," *Philosphical Magazine*, vol. 18, no. 154, p. 773â&, 1968.

[36] A. Garg, A. Hasan, and C. Maloney, "Universal scaling laws for homogeneous disocation nucleation during nano-indentation," in preparation.

[37] A. Acharya, "Constitutive analysis of finite deformation field dislocation mechanics," *Journal of the Mechanics and Physics of Solids*, vol. 52, no. 2, p. 301â316, 2004.

[38] A. Acharya, "Jump condition for GND evolution as a constraint on slip transmission at grain boundaries," *Philosphical Magazine*, vol. 87, no. 8-9, p. 1349â1359, 2007.

[39] A. Acharya, "Microcanonical entropy and mesoscale dislocation mechanics and plasticity," *Journal of Elasticity*, vol. 104, no. 1-2, pp. 23–44, 2011.

[40] A. Acharya, A. Beaudoin, and R. Miller, "New perspectives in plasticity theory: Dislocation nucleation, waves, and partial continuity of plastic strain rate," *Mathematics and Mechanics of Solids*, vol. 13, no. 3-4, p. 292â315, 2008.

[41] J. R. Willis, "Hertzian contact of anisotropic bodies," *Journal of the Mechanics and Physics of Solids*, vol. 14, pp. 163–176, May 1966.

[42] R. Phillips, *Crystals, Defects and Microstructures: Modeling Across Scales*. Cambridge: Cambridge University Press, 2001.

[43] R. Hill, "Aspects of invariance in solid mechanics," *Advances in applied mechanics*, vol. 18, pp. 1–75, 1978.

Appendix A

Hessian matrix calculation for Ercolessi - Adams (EAM) Al. Potential

The total energy E_i of an atom I is given by

$$E_i = F\Big(\sum_{j\neq i}\rho(r_{ij})\Big) + \frac{1}{2}\sum_{j\neq i}\phi(r_{ij}) \tag{A.1}$$

where F is the embedding energy which is a function of the atomic density ρ, ϕ is a pair potential interaction. F, ρ and ϕ are given in discrete form. To interpolate we use cubic spline interpolation and calculate derivatives of the interpolated energy function for computing the forces and hessian. The cubic interpolation function, y(x)

is of the form:

$$y = ax^3 + bx^2 + cx + d \tag{A.2}$$

For given (x_i,y_i) where i = 1, ... ,n are n points, the coefficients of this third order polynomial are calculated using the following algorithm.

$$\begin{aligned} c(i) &= \Big((y(n-2) - y(n+2)\Big) + 8/12\Big((y(n+1) - y(n-1)\Big) \\ b(i) &= 3\Big((y(n+1) - y(n-1)\Big) - 2c(i) - c(i+1) \\ a(i) &= c(i) + c(i+1) - 2\Big((y(n+1) - y(n-1)\Big) \\ d(i) &= y(i) \end{aligned} \tag{A.3}$$

The boundary conditions used are:

$$\begin{aligned} c(1) &= y(2) - y(1) \\ c(2) &= 0.5\Big(y(3) - y(1)\Big) \\ c(n-1) &= 0.5\Big(y(n) - y(n-2)\Big) \\ c(n) &= y(n) - y(n-1) \\ a(n) &= 0, b(n) = 0 \end{aligned} \tag{A.4}$$

A.1 Calculation of Force

For i^{th} atom τ_i is defined as:

$$\tau_i = \sum_{j \neq i} \rho(r_{ij}) \tag{A.5}$$

$$E_{total} = \sum_i E_i \tag{A.6}$$

$$\vec{f_i} = -\vec{\nabla}_{r_i} E_{total} = -\vec{\nabla}_{r_i} \left(F(\tau_i) + \sum_{j \neq i} F(\tau_j) + \sum_{j \neq i} \phi_{ij}(r_{ij}) \right) \tag{A.7}$$

$$= -\sum_{j \neq i} \left(\frac{\partial F(\tau)}{\partial \tau}|_{\tau=\tau_i} \frac{\partial \rho(r)}{\partial r}|_{r=r_{ij}} + \frac{\partial F(\tau)}{\partial \tau}|_{\tau=\tau_j} \frac{\partial \rho(r)}{\partial r}|_{r=r_{ij}} + \frac{\partial \phi_{ij}}{\partial r}|_{r=r_{ij}} \right) \tag{A.8}$$

A.2 Calculation of Hessian

$$\sum_i E_i = \sum_i \left[F\left(\sum_{j \neq i} \rho(r_{ij}) \right) + \frac{1}{2} \sum_{j \neq i} \phi(r_{ij}) \right] = U_{eam} + U_{pair} \tag{A.9}$$

Using cubic spline interpolation,

$$F\left(\sum_{j\neq i}\rho(r_{ij})\right) = F(\tau_i) = \sum_{p=0}^{3} c_p(\tau_i)^p$$
$$U_{eam} = \sum_i \sum_{p=0}^{3} c_p(\tau_i)^p \tag{A.10}$$

$$H^{ij}_{\alpha\beta} = -\frac{\partial^2 U_{eam}}{\partial x^j_\beta \partial x^i_\alpha} = A^{ij}_{\alpha\beta} + B^{ij}_{\alpha\beta} \tag{A.11}$$

$$A^{ij}_{\alpha\beta} = p\chi_1^{ij}\left(\left(\frac{\rho^{ij}_{rr}}{(r^{ij})^2} - \frac{\rho^{ij}_r}{(r^{ij})^3}\right) r^{ij}_\alpha r^{ij}_\beta + \delta_{\alpha\beta}\frac{\rho^{ij}_r}{(r^{ij})}\right)$$
$$A^{ii}_{\alpha\beta} = p\sum_{m\neq i}\chi_1^{mi}\left(\left(\frac{\rho^{mi}_{rr}}{(r^{mi})^2} - \frac{\rho^{mi}_r}{(r^{mi})^3}\right) r^{mi}_\alpha r^{mi}_\beta + \delta_{\alpha\beta}\frac{\rho^{mi}_r}{(r^{mi})}\right) \tag{A.12}$$
$$where, \chi_1^{ij} = \left(\left(\sum_{l\neq i}\rho^{il}\right)^{p-1} + \left(\sum_{l\neq j}\rho^{jl}\right)^{p-1}\right)$$

$$
\begin{aligned}
B^{ij}_{\alpha\beta} = p(p-1)\sum_{m\neq i,j}\Bigg(\Big(\phi^{mi}_r\frac{r^{mi}_\alpha}{r_{mi}}\Big)\Big(\sum_{p\neq m}\phi^{mp}\Big)^{p-2}\Big(\phi^{mj}_r\frac{r^{mj}_\beta}{r_{mj}}\Big)\Bigg) \\
+p(p-1)\Bigg(\Big(\phi^{ji}_r\frac{r^{ji}_\alpha}{r_{ji}}\Big)\Big(\sum_{q\neq j}\phi^{jq}\Big)^{p-2}\Big(\sum_{l\neq j}\phi^{lj}_r\frac{r^{lj}_\beta}{r_{lj}}\Big)\Bigg) \\
+p(p-1)\Bigg(\Big(\sum_{n\neq i}\phi^{ni}_r\frac{r^{ni}_\alpha}{r_{ni}}\Big)\Big(\sum_{q\neq i}\phi^{iq}\Big)^{p-2}\Big(\phi^{ij}_r\frac{r^{ij}_\beta}{r_{ij}}\Big)\Bigg) \qquad \text{(A.13)} \\
B^{ii}_{\alpha\beta} = p(p-1)\sum_{m\neq i}\Bigg(\Big(\phi^{mi}_r\frac{r^{mi}_\alpha}{r_{mi}}\Big)\Big(\sum_{p\neq m}\phi^{mp}\Big)^{p-2}\Big(\phi^{mi}_r\frac{r^{mi}_\beta}{r_{mi}}\Big)\Bigg) \\
+p(p-1)\Bigg(\Big(\sum_{m\neq i}(\phi^{im}_r\frac{r^{im}_\alpha}{r_{im}}\Big)\Big(\sum_{p\neq i}\phi^{i}\Big)^{p-2}\Big(\sum_{l\neq i}\phi^{il}_r\frac{r^{il}_\beta}{r_{il}}\Big)\Bigg)
\end{aligned}
$$

Appendix B

Local strain calculation in Phonon Stability Analysis

The local strain is calculated as given in [23]. The local strain ϵ_{ij} for an atom is used to homogeneously deform the initial crystal. ϵ_{ij} is defined such that the mean square difference between the actual displacements and displacements in the homogeneously deformed crystal of neighbors of the atom of interest is minimum. The expression for ϵ_{ij} is given below.

$$
\begin{aligned}
X_{ij} &= \sum_n \Big(r_n^i(t) - r_0^i(t)\Big)\Big(r_n^j(0) - r_0^j(0)\Big) \\
Y_{ij} &= \sum_n \Big(r_n^i(0) - r_0^i(0)\Big)\Big(r_n^j(0) - r_0^j(0)\Big) \\
\epsilon_{ij} &= \sum_k X_{ik} Y_{jk}^{-1} - \delta_{ij}
\end{aligned}
\tag{B.1}
$$

where i and j represent spatial components of the position of n^{th} atom in the current configuration. $n = 0$ is the atom of interest and $t = 0$ corresponds to the initial configuration.

Appendix C

Young's Modulus Calculation for triangular lattice

The 2D hexagonal crystal considered in this work is isotropic so that the elastic constants take only two independent values. The stress-strain relationship for an isotropic material is given by: $\sigma_{ij} = 2\mu\epsilon_{ij} + (K - \mu)\epsilon_{ii}$ where K is the bulk modulus and μ is the shear modulus. The Young's Modulus, E, and Poisson's ratio, ν, in terms of K and μ can be expressed as:

$$\begin{aligned} \nu &= \frac{K - \mu}{2K} \\ E &= \frac{\mu(3K - \mu)}{K} \end{aligned} \tag{C.1}$$

For pair potentials the bulk modulus, K, and the shear modulus, u, are given by:

$$
\begin{aligned}
C^{Born}_{\alpha\beta\kappa\chi} &= 1/A \sum_{ij} (r_{ij} c_{ij} - t_{ij}) r_{ij} n^{\alpha}_{ij} n^{\beta}_{ij} n^{\kappa}_{ij} n^{\chi}_{ij} \\
K &= 1/4(C_{xxxx} + C_{xxyy} + C_{yyxx} + C_{yyyy}) \\
\mu &= 1/4(C_{xyxy} + C_{xyyx} + C_{yxyx} + C_{yxxy})
\end{aligned}
\tag{C.2}
$$

where n_{ij} is the normalized vector between pair of particles, t_{ij} is the bond tension and c_{ij} is the bond stiffness. For EAM potential we compute E numerically by applying a small ϵ_{yy} to the initial stress free crystal using an indenter with free boundary conditions in the x direction. The emperical relations used to compute E for this case are:

$$
\begin{aligned}
\nu &= \epsilon_{xx}/(\epsilon_{xx} - \epsilon_{yy}) \\
E &= \sigma_{yy}(1 - \nu^2)/\epsilon_{yy}
\end{aligned}
\tag{C.3}
$$